

# Exploring Cosmic Dawn with PANORAMIC I: The Bright End of the UVLF at $z \sim 9 - 17$

ANDREA WEIBEL,<sup>1</sup> PASCAL A. OESCH,<sup>1,2,3</sup> CHRISTINA C. WILLIAMS,<sup>4,5</sup> CHRISTIAN KRAGH JESPERSEN,<sup>6</sup>  
MARKO SHUNTOV,<sup>2,3,1</sup> KATHERINE E. WHITAKER,<sup>7,2</sup> HAKIM ATEK,<sup>8</sup> RACHEL BEZANSON,<sup>9</sup> GABRIEL BRAMMER,<sup>2,3</sup>  
IRYNA CHEMERYNSKA,<sup>10</sup> AIDAN P. CLOONAN,<sup>7</sup> PRATIKA DAYAL,<sup>11,12</sup> LUKAS J. FURTAK,<sup>13</sup> ANNE HUTTER,<sup>14</sup> ZHIYUAN JI,<sup>5</sup>  
MICHAEL V. MASEDA,<sup>15</sup> AND MENGYUAN XIAO<sup>1</sup>

<sup>1</sup>Department of Astronomy, University of Geneva, Chemin Pegasi 51, 1290 Versoix, Switzerland

<sup>2</sup>Cosmic Dawn Center (DAWN), Denmark

<sup>3</sup>Niels Bohr Institute, University of Copenhagen, Jagtvej 128, København N, DK-2200, Denmark

<sup>4</sup>NSF National Optical-Infrared Astronomy Research Laboratory, 950 North Cherry Avenue, Tucson, AZ 85719, USA

<sup>5</sup>Steward Observatory, University of Arizona, 933 North Cherry Avenue, Tucson, AZ 85721, USA

<sup>6</sup>Department of Astrophysical Sciences, Princeton University, Princeton, NJ 08544, USA

<sup>7</sup>Department of Astronomy, University of Massachusetts, Amherst, MA 01003, USA

<sup>8</sup>Institut d'Astrophysique de Paris, CNRS, Sorbonne Université, 98bis Boulevard Arago, 75014 Paris, France

<sup>9</sup>Department of Physics and Astronomy and PITT PACC, University of Pittsburgh, Pittsburgh, PA 15260, USA

<sup>10</sup>Institut d'Astrophysique de Paris, CNRS, Sorbonne Université, 98bis Boulevard Arago, 75014, Paris, France

<sup>11</sup>Kapteyn Astronomical Institute, University of Groningen, PO Box 800, 9700 AV Groningen, The Netherlands

<sup>12</sup>Canadian Institute for Theoretical Astrophysics, 60 St George St, University of Toronto, Toronto, ON M5S 3H8, Canada

<sup>13</sup>Physics Department, Ben-Gurion University of the Negev, P.O. Box 653, Be'er-Sheva 84105, Israel

<sup>14</sup>Department of Astrophysics, University of Vienna, Türkenschanzstraße 17, 1180 Vienna, Austria

<sup>15</sup>Department of Astronomy, University of Wisconsin-Madison, Madison, WI 53706, USA

## ABSTRACT

In its first two years of operation, the James Webb Space Telescope has enabled the discovery of a surprising number of UV-bright galaxies at  $z \sim 10 - 14$ . Their number density is still relatively uncertain, due to cosmic variance effects, and the limited survey area with deep imaging. Here, we combine pure parallel imaging from the PANORAMIC survey with data from legacy fields to constrain the bright end ( $M_{UV} < -18.5$ ) of the UV luminosity function (UVLF) over  $0.28 \text{ deg}^2$  of NIRCам imaging in 6 or more filters, and along 35 independent lines of sight. Using conservative color selections, we compile robust dropout samples at  $z \sim 10$ ,  $z \sim 13$ , and  $z \sim 17$ , and identify 16 new candidates from PANORAMIC. Our inferred UVLFs at  $z \sim 10$  are consistent with literature results and we confirm the high abundance of galaxies at the bright end ( $M_{UV} \lesssim -21$ ) with better number statistics. We find somewhat lower number densities at  $z \sim 13$  compared to previous studies, and no robust candidates at  $z \sim 17$ , indicating a rapid evolution of the galaxy population from  $z \sim 10 - 17$ . The improved upper limits at  $z \sim 17$  imply that the cosmic UV luminosity density drops by at least a factor  $\sim 50$  from  $z \sim 10$  to  $z \sim 17$ . Comparing our results to models proposed to explain the abundance of UV-bright galaxies at  $z \gtrsim 10$ , we conclude that a modest increase in the star formation efficiency, or in the burstiness of star formation, a more top-heavy initial mass function, a lack of dust attenuation, or a combination of these effects at  $z \gtrsim 10$ , is sufficient to match our observational constraints.

**Keywords:** High-redshift galaxies (734), Galaxies (573), Luminosity function (942), Galaxy evolution (594), James Webb Space Telescope (2291), Galaxy photometry (611)

## 1. INTRODUCTION

Characterizing the build-up of the first galaxies that ended the Dark Ages and illuminated the Universe for the first time is one of the key goals of the James Webb Space Telescope (JWST; [Gardner et al. 2023](#)). Prior to the era of JWST observations, the study of the highest

redshift galaxies was limited by the wavelength coverage of the Wide Field Camera 3 (WFC3) onboard the Hubble Space Telescope (HST), probing  $\lambda_{\text{obs}} \lesssim 1.6 \mu\text{m}$ . In principle, it enabled the detection of galaxies out to redshifts of  $z \sim 12$ , at which point the Lyman break starts shifting out of even the reddest WFC3 filter, the

H-band (F160W). [Bouwens et al. \(2011\)](#) identified a candidate galaxy at  $z > 10$ , whose high redshift nature was debated in the literature ([Ellis et al. 2013](#); [Brammer et al. 2013](#)), and that was confirmed to be at  $z_{\text{spec}} = 11.58 \pm 0.05$  with JWST/NIRSpec in [Curtis-Lake et al. \(2023\)](#). Pre-JWST candidates for even higher redshift galaxies based on ground-based and Spitzer/IRAC near-infrared imaging searches ([Harikane et al. 2022](#)) turned out to be at  $z < 5$  with JWST spectroscopy ([Harikane et al. 2025](#)). The highest redshift galaxy with a Lyman break detected in HST slitless grism spectroscopy was GN-z11 ([Oesch et al. 2016](#)), later found to be at  $z = 10.6$  with JWST ([Bunker et al. 2023](#)). However, only a small number of robust galaxy candidates were known at  $z \gtrsim 9$ , making determinations of the UV luminosity function (UVLF) challenging, with some papers suggesting a rapid decline in the number density of objects beyond  $z \sim 9$  (e.g. [Bouwens et al. 2016](#); [Ishigaki et al. 2018](#); [Oesch et al. 2018](#)), and others finding a more shallow evolution (e.g. [McLeod et al. 2016](#)). With the NIRCcam instrument mounted on JWST ([Rieke et al. 2023](#)), the accessible wavelength range has been extended to  $\sim 5 \mu\text{m}$  at comparable spatial resolution and sensitivity, meaning that Lyman Break Galaxies (LBGs) of similar apparent magnitudes can in principle be identified out to  $z > 20$ .

Not only has the redshift record been broken multiple times in the first three years of JWST observations, with spectroscopic confirmations now out to  $z \sim 14$  ([Curtis-Lake et al. 2023](#); [Carniani et al. 2024a](#); [Naidu et al. 2025](#)), but JWST has also revealed a surprisingly high number of luminous  $z \gtrsim 10$  galaxies compared to extrapolations of lower redshift UVLFs, and theoretical expectations (e.g. [Dayal et al. 2014](#); [Mason et al. 2015](#); [Tacchella et al. 2018](#); [Williams et al. 2018](#); [Behroozi et al. 2019](#)). These galaxies were first identified as candidates from imaging data (e.g. [Naidu et al. 2022a](#); [Castellano et al. 2022](#); [Adams et al. 2023](#); [Finkelstein et al. 2023](#); [Atek et al. 2023](#); [Casey et al. 2024](#); [Hainline et al. 2024](#)), and some were later confirmed spectroscopically (e.g. [Arrabal Haro et al. 2023](#); [Castellano et al. 2024](#); [Fujimoto et al. 2024](#); [Harikane et al. 2024](#)).

As a consequence, recently derived UVLFs at  $z \sim 10 - 15$  show an excess at the bright end, and indicate a shallow evolution of the UV luminosity density with respect to pre-JWST expectations (e.g. [Donnan et al. 2023](#); [Pérez-González et al. 2023](#); [Harikane et al. 2023](#); [Adams et al. 2024](#); [Finkelstein et al. 2024](#); [Robertson et al. 2024](#); [Donnan et al. 2024](#); [Whitler et al. 2025](#)). While some photometric candidates contributing to these UVLFs still await spectroscopic confirmation, the high number density at the bright end of the

UVLF is seen from sources with spectroscopic redshifts only out to  $z \sim 13$  ([Harikane et al. 2024](#)). This finding has sparked an extensive debate on its possible causes in the literature. Frequently discussed theoretical explanations include higher star formation efficiencies at high redshift ([Dekel et al. 2023](#); [Li et al. 2024](#); [Boylan-Kolchin 2024](#); [Mauerhofer et al. 2025](#)), a lack of dust attenuation ([Ferrara et al. 2023](#)), bursty star formation histories ([Mason et al. 2023](#); [Shen et al. 2023](#); [Sun et al. 2023](#); [Kravtsov & Belokurov 2024](#)), and a more top heavy initial mass function (IMF) with increasing redshift and/or in highly star-forming regions ([Yung et al. 2024](#); [Trinca et al. 2024](#); [Cueto et al. 2024](#); [Lu et al. 2025](#); [Mauerhofer et al. 2025](#); [Hutter et al. 2025](#)). Other authors also explored helium enhancement and nebular continuum emission ([Katz et al. 2024](#)), a contribution of AGN to the observed UV-luminosity ([Pacucci et al. 2022](#); [Hegde et al. 2024](#)), or larger dust grain sizes ([Toyouchi et al. 2025](#); [Narayanan et al. 2025](#)) as possible drivers of the observed abundance of UV-bright galaxies at  $z \gtrsim 10$ .

Despite all this ongoing discussion, galaxy sample sizes remain small at the bright end of the UVLF at  $z \gtrsim 10$  due to the limited survey area that has been imaged with JWST at sufficient depth and wavelength resolution. Further, most determinations of the UVLF based on early JWST data rely on a small number of independent lines of sight, meaning that they are subject to significant cosmic variance, i.e., variations in the measured number density of galaxies due to the clustering of dark matter halos and galaxies in the cosmic web (e.g. [Moster et al. 2011](#); [Jespersen et al. 2025](#)). Indeed, studies based on imaging along a larger number of independent sightlines somewhat mitigated earlier findings. [Willott et al. \(2024\)](#) analysed data along 5 independent lines of sight from the CANadian NIRISS Unbiased Cluster Survey (CANUCS, [Willott et al. 2022](#)), and found a much steeper decline in the space density of UV-selected galaxies from  $z \sim 8 - 12$  relative to other early JWST studies, with no candidates at  $z > 12.5$ . Using the first 19 fields from the pure-parallel program Bias-free Extragalactic Analysis for Cosmic Origins with NIRCam (BEACON), [Morishita et al. \(2025\)](#) found moderate number densities of galaxies at  $z \sim 10 - 13$  compared to previous results, and no robust candidates at  $z > 13$  resulting in upper limits that are just consistent or even below previous determinations of the UVLF. Cosmic variance effects are also emphasized in a recent paper from [Asada et al. \(2025\)](#) who derived the UVLF at  $10 < z < 16$  from deep medium and wide-band imaging in three independent NIRCcam-pointings from CANUCS and the JWST in Technicolor program (GO-3362, PI Muzzin) and found that it is 0.6 dex lower than the

UVLF measured in the JADES Origins Field with similar NIRCcam coverage (Robertson et al. 2024). Complementarily, Rojas-Ruiz et al. (2024) used a sample of spectroscopically confirmed galaxies from the BoRG-JWST survey (Roberts-Borsani et al. 2024a), previously identified from pure-parallel HST-imaging along  $> 200$  independent lines of sight, and found higher number densities of UV-luminous galaxies at  $z \sim 7 - 9$ , compared to estimates based on JWST legacy fields, which may alleviate the implied shallow evolution of the bright end of the UVLF with redshift out to  $z \gtrsim 10$ .

These results illustrate the need for a large number of independent lines of sight to obtain an unbiased view of the evolution of the UVLF and the build-up of galaxies at Cosmic Dawn (see e.g., Trapp et al. 2022). Such data can be provided by JWST/NIRCcam pure parallel imaging, as collected in Cycle 1 by the Parallel wide-Area Nircam Observations to Reveal And Measure the Invisible Cosmos (PANORAMIC, Williams et al. 2025).

Efficient selection of high redshift galaxies through the Lyman break technique (e.g. Steidel et al. 1996; Madau et al. 1996) is constrained to redshift ranges that are feasible for the photometric filters of a given survey. In the case of PANORAMIC imaging, those are the short-wavelength (SW) channel filters F115W, F150W, and F200W, probing wavelengths of  $\sim 1 - 2\mu\text{m}$ . While a large number of high-redshift candidates have been identified and confirmed through F115W and F150W dropouts ( $z \sim 9 - 11$  and  $z \sim 12 - 14$  respectively), F200W dropouts remain rare, and some seemingly robust candidates have turned out to be transients or lower redshift interlopers. For example, a  $z \sim 16$  candidate from Hainline et al. (2024, with weak detected flux in F200W), has turned out to be a supernova (DeCoursey et al. 2025). The most prominent example, however, is the so-called Schrödinger galaxy. First identified as a bright and robust  $z \sim 16.6$  candidate in CEERS imaging (Naidu et al. 2022a; Harikane et al. 2023; Donnan et al. 2023), this source turned out to be a  $z = 4.9$  dusty starburst galaxy (Arrabal Haro et al. 2023), as already suggested in Naidu et al. (2022b) and Zavala et al. (2023).

Recently, candidate galaxies at  $z \gtrsim 15$  have been identified in the deepest available JWST imaging over small fields (Kokorev et al. 2024a; Pérez-González et al. 2025). These candidates are relatively faint ( $M_{\text{UV}} \gtrsim -19$ ), making their spectroscopic confirmation challenging. Castellano et al. (2025) performed a careful search for  $z \gtrsim 15$  galaxies over  $\sim 0.2\text{deg}^2$  of legacy imaging, and identified 9 brighter candidates ( $M_{\text{UV}} \lesssim -19$ ) at  $z \sim 15 - 20$ . However, as they discuss, two additional sources that satisfy their selection criteria, and have

NIRSpec spectroscopy turn out to be low-redshift interlopers, and different photometric redshift codes identify secondary low-redshift solutions for all of their candidates.

Here, we use imaging data from PANORAMIC, in combination with publicly available NIRCcam imaging in various legacy fields to select F115W, F150W, and F200W dropouts and estimate the bright end of the UVLF at  $z \gtrsim 9$  based on 35 independent lines of sight covering a total area of  $1020\text{arcmin}^2$ , or  $0.28\text{deg}^2$  – the largest survey area with deep JWST imaging data in 6 or more filters used to construct a UVLF to date. We further leverage the large number of independent sight-lines to perform a measurement of cosmic variance and through it the galaxy bias at  $z \sim 10$  in an upcoming paper (Weibel & Jespersen et al. in prep.).

This paper is structured as follows. We present an overview of the imaging data, describe the photometric catalogs, the sample selection, the spectral energy distribution (SED) fitting, as well as our determination of sample completeness and our calculation of the UVLF with its uncertainties in Section 2. In Section 3, we present our results, starting with a discussion of each of the three samples and some new and outstanding candidates, followed by a comparison of our UVLFs and the inferred UV luminosity density with the literature, as well as various models and simulations. We discuss our findings in Section 4, and conclude in Section 5.

Throughout this work, we assume a  $\Lambda$ CDM cosmology with parameters from the nine-year Wilkinson Microwave Anisotropy Probe Observations (Hinshaw et al. 2013),  $h = 0.6932$  and  $\Omega_{m,0} = 0.2865$ . All magnitudes are reported in the AB system.

## 2. DATA AND METHODS

### 2.1. Imaging

The basis of this work are the publicly available imaging data from JWST and HST from various legacy surveys, as well as the PANORAMIC pure parallel data. All imaging mosaics have been consistently reduced through the *grizli* software package (Brammer 2023a), starting from level 2 calibrated data products from the Mikulski Archive for Space Telescopes (MAST), as outlined in e.g., Valentino et al. (2023). We use JWST imaging data in the following fields: (1) in the EGS with data from the Cosmic Evolution Early Release Science Survey (CEERS, ERS-1345, PI Finkelstein, Finkelstein et al. 2025), GO-2279 (PI Naidu), DDT-2750 (PI Arrabal-Haro), and GO-2234 (PI Banados); (2) in the UDS and COSMOS fields with data from the Public Release Imaging for Extragalactic Research (PRIMER, GO-1837, PI Dunlop, see, e.g., Donnan

et al. 2024), COSMOS-Web (GO-1727, PIs Kartaltepe & Casey, Casey et al. 2023), GO-1810 (PI Belli), GO-1840 (PI Alvarez-Marquez), and DDT-6585 (PI Coulter); (3) in the GOODS fields (North and South) with data from the JWST Advanced Deep Extragalactic Survey (JADES, GTO-1180 & GTO-1181, PI Eisenstein, as well as GTO-1210, PI Luetzgendorf, Eisenstein et al. 2023a), First Reionization Epoch Spectroscopically Complete Observations (FRESCO, GO-1895, PI Oesch, Oesch et al. 2023), Complete NIRCcam Grism Redshift Survey (CONGRESS, GO-3577, PIs Egami & Sun), GO-2079 (PI Finkelstein), the JWST Extragalactic Medium-band Survey (JEMS, GO-1963, PIs Williams, Maseda & Tacchella, Williams et al. 2023), the JADES Origins Field (GO-3215, PI Eisenstein, Eisenstein et al. 2023b), GTO-1264 (PI Robledo), GO-4762 (PI Fujimoto), and Slitless Areal Pure-Parallel High-Redshift Emission Survey (SAPPHIRES, GO-6434, PI Egami); (4) the Abell-2744 cluster with data from Ultra-deep NIRCcam and NIRSpec Observations Before the Epoch of Reionization (UNCOVER, PIs Labbé & Bezanson, Bezanson et al. 2024), GLASS (ERS-1324, PI Treu, Treu et al. 2022), DDT-2756 (PI Chen), All the Little Things (ALT, GO-3516, PIs Naidu & Matthee, Naidu et al. 2024), and Medium bands, Mega Science (GO-4111, PI Suess, Suess et al. 2024); (5) the JWST North Ecliptic Time-Domain Field with data from Prime Extragalactic Areas for Reionization and Lensing Science (PEARLS, GTO-2738, PIs Windhorst & Hammel, Windhorst et al. 2023).

As an important extension, we include data from the PANORAMIC survey (GO-2514, PIs Williams & Oesch, Williams et al. 2025), grouped in 39 associations (i.e., imaging mosaics). Most of these contain a single NIRCcam pointing with imaging in six wide filters (F115W, F150W, F200W, F277W, F356W, and F444W) with a few deep pointings having additional data in the F410M band, and a few associations containing multiple pointings. Of the 39 associations, 9 overlap with or are in close proximity to the UDS, COSMOS or one of the GOODS fields, adding depth and/or area to those legacy fields. For full details on the survey design and data reduction of PANORAMIC, see Williams et al. (2025). In total, PANORAMIC provides imaging in 6 or more filters over  $432 \text{ arcmin}^2$ , of which  $\sim 250 \text{ arcmin}^2$  are split over 28 independent and new lines of sight (at  $> 2 \text{ deg}$  separation from other fields).

In addition, the cycle 2 pure parallel program BEACON (GO-3990, PIs Morishita, Mason, Treu & Trenti, Morishita et al. 2025) contributes imaging to the mosaics in the EGS, UDS, and Abell-2744 fields.

We use version 7.0 or higher imaging products from the DAWN JWST Archive (DJA)<sup>1</sup> in all the legacy fields, as well as version 7.2 mosaics from the first PANORAMIC data release<sup>2</sup>.

We additionally modify the science mosaics in the Abell-2744 field to remove the brightest cluster galaxies (BCGs). To this end, we compute a running median filter with a box-size of  $101 \times 101$  pixels ( $4.04'' \times 4.04''$ ) and subtract it from the original images.

All the NIRCcam long-wavelength (LW) channel and HST filters are drizzled to a pixel scale of  $0.04''$  while the NIRCcam SW channel filters are usually drizzled to a smaller pixel scale of  $0.02''$  to leverage their higher spatial resolution. Exceptions are the large CEERS and PRIMER mosaics where all filters are drizzled to  $0.04''$ .

## 2.2. Photometric Catalogs

From the uniformly reduced imaging mosaics we generate point spread function (PSF) matched photometric catalogs, following the methods outlined in Weibel et al. (2024) and Williams et al. (2025). To summarize briefly, we generate inverse-variance weighted stacks of the F277W, F356W, and F444W mosaics in each field, and run **SourceExtractor** (Bertin & Arnouts 1996) in dual mode, using the stacks as the detection image, and measuring fluxes through circular apertures with  $0.16''$  radius on PSF matched versions of all available JWST and HST mosaics. These aperture fluxes are scaled to total based on a Kron ellipse determined on the detection image and an additional correction to account for flux in the wings of the PSF, beyond the Kron ellipse.

For most filters in the legacy fields, PSFs are extracted from the images using an automatically generated list of stars and the python tool **psf.EPSFBuilder** (Anderson & King 2000; Anderson 2016) which is part of the **photutils** package (Bradley et al. 2022). However, some filters only cover a small area within a given legacy field, e.g., a single NIRCcam pointing ( $\sim 9.7 \text{ arcmin}^2$ ) which usually does not contain a sufficient number of isolated stars for the construction of an empirical PSF. In such cases, as well as for all the PANORAMIC pointings (most of which are single NIRCcam pointings), we instead use **webbpsf** (Perrin et al. 2014) with a **jitter\_sigma** parameter of 0.02 to derive PSFs, which we further rotate to match the position angle of each observation.

Whenever NIRCcam/SW mosaics are available on a  $0.02''$  pixel scale, we re-bin those mosaics to  $0.04''$  since **SourceExtractor** requires all mosaics to be on the same

<sup>1</sup> <https://dawn-cph.github.io/dja/imaging/v7/>

<sup>2</sup> <https://panoramic-jwst.github.io/>



pixel grid. However, we extract PSFs from the  $0.02''$  images and then re-bin the PSFs to benefit from the more accurate sampling of the strongly centrally peaked radial profiles.

### 2.3. Sample Selection

We proceed with the sample selection, which is mainly based on photometric fluxes and colors, rather than photometric redshifts, simplifying the subsequent treatment of completeness (Section 2.8). Given that we wish to probe the bright end of the UVLF, we choose conservative selection cuts with the goal of obtaining a pure sample that avoids significant contamination of low redshift interlopers.

Our three redshift bins are determined by the wavelength coverage of the NIRCcam/SW filters at  $\lambda > 1 \mu\text{m}$ : F115W, F150W, and F200W. We select dropouts in each of these filters as follows:

#### **F115W dropouts ( $z \sim 10$ )**

$$\begin{aligned} \text{F115W} - \text{F150W} &> 1.5 \quad \wedge \\ \text{F150W} - \text{F356W} &< 0.5 \quad \wedge \\ \text{SNR}(\text{F150W}) &> 8 \quad \wedge \\ \text{SNR}(\text{F200W}) &> 3 \end{aligned} \quad (1)$$

#### **F150W dropouts ( $z \sim 13$ )**

$$\begin{aligned} \text{F150W} - \text{F200W} &> 1.5 \quad \wedge \\ \text{F200W} - \text{F444W} &< 0.5 \quad \wedge \\ \text{SNR}(\text{F200W}) &> 8 \quad \wedge \\ \text{SNR}(\text{F277W}) &> 3 \end{aligned} \quad (2)$$

#### **F200W dropouts ( $z \sim 17$ )**

$$\begin{aligned} \text{F200W} - \text{F277W} &> 1.5 \quad \wedge \\ \text{F277W} - \text{F444W} &< 0.5 \quad \wedge \\ \text{SNR}(\text{F277W}) &> 8 \quad \wedge \\ \text{SNR}(\text{F356W}) &> 3 \end{aligned} \quad (3)$$

where FXXXW refers to the AB-magnitude in the respective filter, and we replace fluxes with  $< 2\sigma$  detections by  $2\sigma$  upper limits before converting to AB-magnitudes. The second SNR-cut (e.g.,  $\text{SNR}(\text{F200W}) > 3$  in the F115W dropout selection) is to remove sources

that only have a high SNR in one filter (typically diffraction spikes or other spurious detections) without biasing against true high- $z$  galaxies with blue SEDs. We further apply the `use_phot` flag from Weibel et al. (2024) which removes a small number of spurious objects and sources that were flagged as stars.

Three reviewers (AW, PO, and CW) then visually inspect two sets of NIRCcam imaging cutouts with stronger and weaker contrast as well as the photometric fluxes of all candidates. We do not inspect any SED-fitting output to avoid being influenced by the preferred solution of an SED-fitting code, and we mainly remove artifacts (e.g., diffraction spikes and hot pixels), and sources with image quality issues or contaminated photometry. We further remove objects with clearly visible flux in filters probing wavelengths below the supposed Lyman break, usually the NIRCcam filter just blue-wards of the break, i.e., F150W, F115W, and F090W for the F200W, F150W, and F115W dropouts. We note here that F090W is not available in all fields, and refer to a more general discussion of the effect of the inhomogeneous filter coverage across fields in Section 4.1.1.

During visual inspection, we noticed a number of candidates that nominally satisfy the selection cuts, and are real sources with unproblematic photometry, but whose SED is either too blue to be fit with a reasonable UV-continuum, or suspiciously red, in combination with a smooth turn-over around the supposed Lyman break. These sources can be reliably identified to be emission line or Balmer break galaxies at  $z \lesssim 5$  through SED-fitting. In order not to significantly bias our color selection, we only remove sources that are fit at low redshift with very high confidence using our standard `eazy` setup (see Section 2.4). Specifically, we remove sources with  $P(z < 8.5) > 0.95$ , i.e., with a  $> 95\%$  probability of being at a redshift  $< 8.5$  according to the `eazy` redshift probability distribution.

In the F115W dropout sample, we selected two out of three images of the triply imaged  $z \sim 10$  candidate first published in Zitrin et al. (2014), and with spectroscopic redshifts from UNCOVER and the DDT program DD-2756 (PI Chen, Chen et al. 2022). We remove the fainter of the two images to avoid double-counting the source and are left with final sample sizes of 86 F115W dropouts, 11 F150W dropouts and 4 F200W dropouts.

Further, 10 objects in total (6 F115W dropouts, 3 F150W dropouts and 1 F200W dropout) have aperture correction factors  $> 3$  (see Section 2.2). In all cases, this is due to the Kron ellipse being contaminated by a bright neighboring galaxy. We re-measure the total fluxes of those 10 objects by multiplying their aperture fluxes by the median aperture correction and dividing

by the median encircled energy of the Kron ellipse on the F444W PSF measured from all our sample galaxies, resulting in a total correction factor of 1.87. While the resulting total fluxes may not be accurate depending on the morphology of the sources, we argue this effect should be minimal as both the affected galaxies and most of the sample are compact.

Finally, we determine the nominal redshift range of each sample based on the NIRCcam filter throughput curves. We assume a flat SED in  $f_\nu$  ( $\beta = -2$ ), with a sharp Lyman break, i.e.,  $f_\nu(\lambda) = C = \text{const.}$ , if  $\lambda_{\text{rest}} > 1216\text{\AA}$  and  $f_\nu = 0$  if  $\lambda_{\text{rest}} < 1216\text{\AA}$ . Shifting this SED to higher and higher redshift, we measure the synthetic fluxes in the NIRCcam bands, and determine the redshift at which the flux in the first dropout filter, F115W, drops to  $C/2$ , due to the Lyman break entering that filter. This marks the lower end of our lowest redshift bin. Nominally, our selection with a color  $F115W - F150W > 1.5$  corresponds to a factor of  $\sim 4$  in  $f_\nu$ , but the factor of 2 generously accounts for noise in both filters. Shifting the synthetic SED to even higher redshifts, the Lyman break starts to enter F150W, decreasing the measured color. We then determine the redshift at which the flux in F150W drops to  $C/2$  as both the upper bound on the lowest redshift bin, and the lower bound of the second redshift bin (F150W dropouts), and repeat this process for the F200W dropouts. This yields nominal ranges of  $8.6 < z < 11.3$ ,  $11.3 < z < 15.3$ , and  $15.3 < z < 21.9$  for the F115W, F150W, and F200W dropout samples respectively.

#### 2.4. Photometric Redshifts

We run the template-based SED-fitting code **eazy** (Brammer et al. 2008) to estimate photometric redshifts using the **blue\_sfhz** template set<sup>3</sup> which consists of 13 templates with redshift-dependent properties generated through the Flexible Stellar Population Synthesis (FSPS) code (Conroy et al. 2009; Conroy & Gunn 2010) and a 14th template based on a strong emission line galaxy at  $z = 8.5$  from Carnall et al. (2023a). In an initial run, we let the redshift vary freely in the range  $z \in (0.01, 20)$  and use the resulting redshift probability distribution  $P(z)$  to remove confident low-redshift interlopers from our sample as described above.

We then re-run **eazy** on each of our three final samples, constraining the redshift to be in the nominal range of our dropout selection as specified in the previous Section, adding (subtracting) 0.1 at the upper (lower) end

of the bin to allow for some additional flexibility. This is based on the idea that our sample selection yields robust high- $z$  galaxies and that we do not want to convolve our selection function with the mechanics of a photometric redshift fitting code, to keep it simple and easier to correct for. In the **eazy** run with free redshift, only 5 of our F115W dropouts, 1 of our F150W dropouts and 1 of our F200W dropouts (see Section 3.1.3) have maximum likelihood solutions at  $z < 5$ , as also listed in Tables 2 and 3 in Appendix A.

#### 2.5. Spectroscopic Redshifts

We match our dropout samples with all JWST-based spectroscopic redshifts on the DJA, finding 25, 2, and 2 matches in the three samples. In addition, our F150W dropout sample contains the second most distant spectroscopically confirmed object, JADES-GS-z14-0 at  $z \sim 14$  (Carniani et al. 2024a), but its spectrum was not available on the DJA as of March 20, 2025. We therefore add its spectroscopic redshift of  $z = 14.1796 \pm 0.0007$  as measured in Carniani et al. (2024b, see also Schouws et al. 2024) to the comparison. To estimate the uncertainty in the spectroscopic redshifts from the DJA, we run **msaexp** (Brammer 2023b) to determine  $\chi^2$  values on a redshift grid covering  $z \in (8, 16)$  in steps of 0.01 and convert those  $\chi^2$  values to a likelihood as  $P(z) = e^{-(\chi^2(z) - \min(\chi^2(z)))/2}$  to infer  $1\sigma$  uncertainties as half the difference between the 84th and the 16th percentile. We plot the available spectroscopic redshifts with their inferred uncertainties against our photometric redshifts from the initial **eazy** run with free redshift in Figure 1. In some cases, the uncertainty of the spectroscopic redshift is larger than the uncertainty of the photometric redshift. This happens if the redshift is only constrained by the Lyman break (and no other features such as rest-UV emission lines), and the SNR of the spectrum is low compared to the photometry.

Remarkably, all except for two of our photometric candidates with available spectra are confirmed to be at high redshift, and the  $z_{\text{phot}}$  estimate from **eazy** is consistent with  $z_{\text{spec}}$  for the vast majority of cases.

The two exceptions are both F200W dropouts. One is the Schrödinger galaxy at  $z_{\text{spec}} = 4.9$  (Arrabal Haro et al. 2023), the other has a spectrum from the CANDELS-Area Prism Epoch of Reionization Survey (CAPERS, GO-6368, PI Dickinson) that also puts it at  $z_{\text{spec}} = 4.9$ . We discuss these sources further in Section 3.1.3.

With JWST measuring spectroscopic redshifts for dozens of galaxies at  $z \gtrsim 10$ , photometric redshift estimates have been found to be biased high at those redshifts. This may be related to an Eddington-type bias as

<sup>3</sup> <https://github.com/gbrammer/eazy-photoz/tree/master/templates/sfhz>

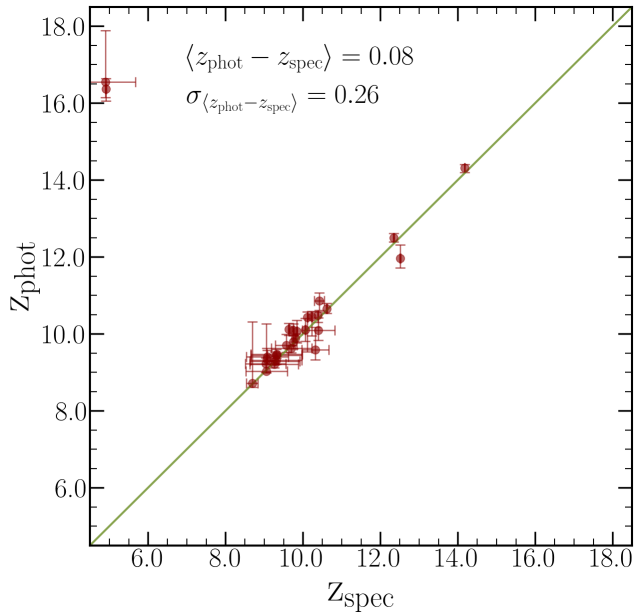


**Figure 1.** Comparison of photometric with spectroscopic redshifts for the 29 galaxies that have a grade 2 (3 cases) or grade 3 (26 cases) spectrum on the DJA (i.e. high-quality), as well as JADES-GS-z14-0 with its spectroscopic redshift from Carniani et al. (2024b). We find that the  $z_{\text{phot}}$  estimate from *eazy* is in excellent agreement with  $z_{\text{spec}}$ , with only two exceptions in the F200W dropout sample that are  $z = 4.9$  strong emission line sources (see text, and Section 3.1.3).

discussed in Serjeant & Bakx (2023), or incorrect modeling of the strong Lyman- $\alpha$  damping wing caused by high neutral hydrogen column densities (Heintz et al. 2025). Interestingly, we only find a marginal mean offset  $\langle z_{\text{phot}} - z_{\text{spec}} \rangle = 0.08$  with a scatter of 0.26, suggesting that with photometry of sufficiently high SNR, redshifts at  $z > 10$  are recovered accurately and with relatively small scatter with the *eazy* setup used here.

One might expect spectroscopically confirmed sources at  $z \gtrsim 9$  to be biased towards the brightest and therefore most robust photometric candidates that were selected from early JWST or HST imaging data, and prioritized in the NIRSpec/MSA mask design. Further, robust spectroscopic redshifts can only be measured from relatively bright sources and/or deep spectra. To test this, we plot  $M_{\text{UV}}$  against redshift for our entire sample of galaxies in Figure 2, highlighting those with spectroscopic redshifts as red stars. A compilation of spectroscopically confirmed objects from Roberts-Borsani et al. (2024b) is shown in the background. Note that this sample is only shown for reference and that it contains sources that are also part of our sample, but with slightly different measured redshifts and  $M_{\text{UV}}$  due to the independent data processing.

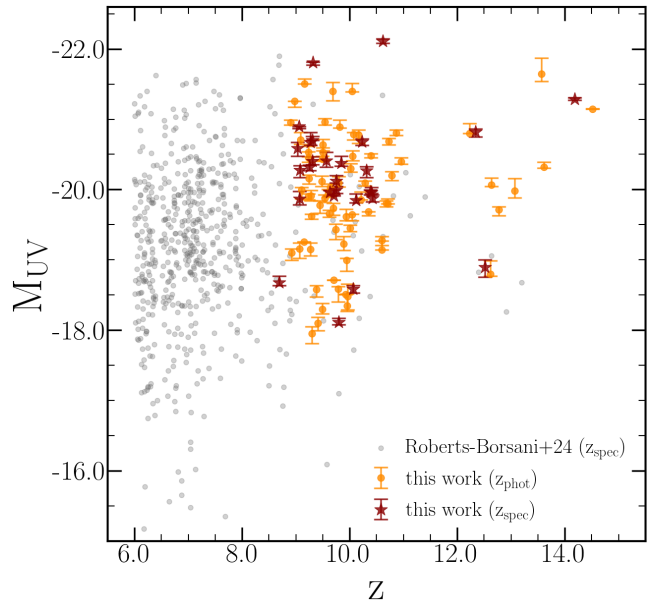


**Figure 2.** Absolute UV-magnitude  $M_{\text{UV}}$  against redshift for all the sample galaxies with (red stars) or without (orange circles) spectroscopic redshifts. This shows that sources with  $z_{\text{spec}}$  are not substantially biased towards the brightest objects, relative to our photometric sample. The grey markers are a compilation of spectroscopically confirmed galaxies from Roberts-Borsani et al. (2024b) shown for reference.

While the spectroscopically confirmed sample does contain some of the brightest sources in the sample at  $z \sim 10$  as well as the brightest source at  $z \sim 14$  (Carniani et al. 2024a,b), the median  $M_{\text{UV}}$  of the sources with  $z_{\text{spec}}$  ( $-19.8$ ) is in fact slightly higher than that of the sources without  $z_{\text{spec}}$  ( $-20.1$ ), indicating that our spectroscopic sample is not substantially biased towards brighter sources. This may be due to the “wedding-cake” nature of the compilation of all the legacy surveys which enabled a robust selection and spectroscopic follow-up of bright high- $z$  candidates from large areas, as well as fainter candidates from deeper imaging over smaller areas.

However, the spectroscopically confirmed sources have somewhat more robust photometric redshifts from *eazy* with a median  $1\sigma$  uncertainty of 0.17, compared to sources without  $z_{\text{spec}}$  that show a median  $1\sigma$  uncertainty of 0.30. This is in part because the spectroscopically confirmed sources mostly lie in legacy fields with relatively deep imaging data in many filters. We discuss this in more detail in Section 4.1.1. The success rate of 100% of our F115W and F150W dropout selection among the spectroscopically confirmed objects therefore likely overestimates the purity of the sample. That said, it is nevertheless re-assuring and confirms that our rather con-

servative selection cuts successfully identify true high redshift galaxies with a low expected interloper fraction.

As an additional test of our selection, we cross-match our full photometric catalog with all grade 3 sources (sources with robust spectroscopic redshifts confirmed through visual inspection) on the DJA with  $z_{\text{spec}} > 8.6$ , and find 53 confirmed high redshift galaxies that are not included in our sample. 38 of them would fall in our F115W dropout sample, but do not satisfy our Lyman break color selection and/or the SNR-cut in F150W. 18 of those sources lie at  $z_{\text{spec}} < 9$ , the lower end of the nominal redshift range of the F115W dropout selection. These sources often have measured Lyman break colors  $< 1.5$ , even if they are relatively bright, because of the Lyman break being in the F115W filter. The other 20 sources are either at the upper end of the redshift range (6 sources at  $z_{\text{spec}} > 10$ ), where the Lyman break enters F150W, or are just too faint to pass our selection. We further find 4 sources that would fall in our F150W dropout sample. All of them have Lyman break colors  $< 1.5$  and are too faint to be included in our sample, either because  $\text{SNR}(\text{F200W}) < 8$  (2 cases), and/or because of the insufficient depth of the F150W imaging to measure a color  $> 1.5$ . All these effects are taken into account in our completeness correction (Section 2.8.2). The remaining 11 sources are not included because of missing or flagged photometry in one or more of the required NIRC2 wide filters which is accounted for in our survey area calculation. This illustrates that our selection is limited to bright sources and/or sufficiently deep photometry, and it highlights the power of NIR-Spec to measure redshifts of relatively faint sources even at  $z > 10$ .

## 2.6. SED-Fitting

To estimate the UV-magnitude  $M_{\text{UV}}$  and -slope  $\beta$  of our sample galaxies, we run the Bayesian Analysis of Galaxies for Physical Inference and Parameter Estimation tool (**bagpipes**; Carnall et al. 2018), fixing the redshift to  $z = z_{\text{eazy}}$  with a Gaussian prior whose width is given by  $(z_{\text{eazy}, 84} - z_{\text{eazy}, 16})/2$ .

We further assume the non-parametric star formation history (SFH) model introduced in Leja et al. (2019) with the bursty continuity prior as described in Tacchella et al. (2022) to account for supposed bursty star formation at high redshifts (e.g., Ciesla et al. 2024; Cole et al. 2023; Looser et al. 2023). The SFH is split into 8 time-bins of which the first three are fixed to 0 – 10, 10 – 30, and 30 – 70 Myr lookback time. The other five bins are set to be equally sized in linear time from 70 Myr lookback time to  $z = 30$ . We use a uniform prior on the metallicity in the range  $Z_* \in (0.01, 1) Z_{\odot}$ .

Our implementation of dust is similar to the setup described in Carnall et al. (2023b). It is based on the model of Salim et al. (2018) with a uniform prior on the absolute attenuation in the V-band,  $A_V \in (0, 1)$ . We further fit for the deviation from the Calzetti et al. (2000) slope,  $\delta \in (-0.3, 0.3)$  with a Gaussian prior centered at 0 and with a dispersion of 0.1, for the strength of the UV-bump at  $2175 \text{ \AA}$   $B \in (0, 5)$  with a uniform prior, and for the multiplicative factor on  $A_V$  for stars in birth clouds (defined to be stars younger than 20 Myr.),  $\eta \in (1, 3)$ , with a uniform prior. While these dust properties are likely degenerate with the SFH and hard to constrain from rest-frame UV photometry, we prefer to allow for flexibility in the fits, and marginalize over possible dust effects on the UV-continuum to get conservative estimates on the uncertainty in  $M_{\text{UV}}$ , and  $\beta$  which, apart from the redshift, are the only SED-fitting derived quantities used in this work.

The stellar population models used in the fitting are from BPASS-v2.2.1 (Stanway & Eldridge 2018) which assumes a broken power-law IMF as described in Eldridge et al. (2017), building on Kroupa et al. (1993). Nebular emission in **bagpipes** is modeled with CLOUDY (Ferland et al. 2017) as described in Carnall et al. (2018), and we fit for the logarithm of the ionization parameter in the range  $\log(U) \in (-4, -1)$  assuming a uniform prior.

**bagpipes** then allows us to measure the UV-properties of each sample galaxy in a Bayesian way. To this end, we first sample 500 realizations of the fitted SED from the posterior distribution. For each realization, we keep track of the fitted redshift, perform a linear regression fit in the range  $1350 \text{ \AA} < \lambda_{\text{rest}} < 2800 \text{ \AA}$  to infer the UV-slope  $\beta$ , and measure the UV-magnitude  $M_{\text{UV}}$  as the mean flux in the range  $1450 \text{ \AA} < \lambda_{\text{rest}} < 1550 \text{ \AA}$ . The median and percentiles of the 500 measurements respectively then constitute our final values and uncertainties of  $M_{\text{UV}}$ ,  $\beta$ , and  $z$ .

## 2.7. Gravitational Magnification in A2744

For the sources in the Abell-2744 field, we correct their measured UV-magnitudes for gravitational lensing magnification. We use the v2.0 UNCOVER string lensing model of the cluster, which was constructed by Furtak et al. (2023) using the Zitrin et al. (2015) analytic method and has recently been updated with new spectroscopic redshifts from JWST in Price et al. (2025). This parametric model, comprising five smooth dark matter halos and 552 cluster galaxies, is constrained with 187 multiple images belonging to 66 sources, 60 of which have spectroscopic redshifts. The model achieves a final average image reproduction error of  $\Delta_{\text{RMS}} = 0.6''$ .



We compute magnifications at each source’s position and redshift. In order to calculate the volume effectively probed in the Abell-2744 field (see Section 2.11), we construct source planes for each redshift bin.

## 2.8. Completeness

While we have shown that it is reasonable to assume that our samples have a high purity, we need to quantify their completeness in order to measure the UVLF. This is aided by the simplicity of our selection which mostly relies on photometric fluxes and colors. We assume here that the removal of confident low redshift interlopers based on *eazy* (see Section 2.3) has no effect on the completeness. We assess completeness in two steps. First, we measure the detection completeness, i.e., the completeness of source detection and extraction with *SourceExtractor*. Then, we measure the selection completeness, i.e., the completeness of our selection cuts, as a function of the redshift, and the rest-UV- and noise properties of our sample galaxies.

### 2.8.1. Detection Completeness

We use the GaLaxy survey Completeness Algorithm 2 (*GLACiAR2*) software (Carrasco et al. 2018; Leethochawalit et al. 2022) to perform injection-recovery simulations. Specifically, we inject model galaxies into the real NIRC*am* images, run *SourceExtractor*, and measure the fraction of recovered galaxies as a function of their input and output magnitude. Given the large size of the EGS, UDS, COSMOS, GOODS-S and GOODS-N fields, we run *GLACiAR2* on  $7.5' \times 7.5'$  cutouts of each image. The cutouts however cover a substantial part of each mosaic, including deeper and shallower parts as well as regions near the edge. We only include the F277W, F356W and F444W mosaics in the simulations, and an inverse-variance weighted stack of the three filters as the detection image.

For each field, we perform 10 iterations with 500 galaxies per iteration. The input galaxies have flat SEDs in  $f_\nu$  ( $\beta = -2$ ), are fixed to be at a redshift of  $z = 10$ , and are injected in 42 magnitude bins ranging from 22.5 to 32.5 AB. An equal number of galaxies is injected in each magnitude bin, but their values of  $M_{UV}$  are sampled from a Schechter function (Schechter 1976) within the bin.

The model galaxies are assumed to have Sérsic light profiles with 25% of the galaxies having Sérsic indices of 1 and 2 respectively, and the remaining 50% having a Sérsic index of 1.5. Their sizes follow a log-normal distribution centered on  $R_{\text{eff}} = 0.36$  kpc. Finally, we use 5 equally sized bins in inclination and eccentricity.

Each simulation yields a matrix specifying the number of recovered sources in each bin of input and output

magnitude. The detection completeness in a bin of output magnitude is then given by a weighted mean over the recovered fraction in each input magnitude bin from which galaxies scattered into that output magnitude bin.

### 2.8.2. Selection Completeness

To assess the completeness of our sample selection (Section 2.3), we roughly follow the methodology outlined in Harikane et al. (2022). For each galaxy in our sample, we create mock SEDs, based on the 500 sets of values of  $M_{UV}$ ,  $\beta$ , and  $z$ , sampled *together* from the *bagpipes* posterior to retain covariance information, and assuming a simple power law shape with a slope  $\beta$ . We apply IGM attenuation to the mock SEDs using the model from Inoue et al. (2014), and convolve them with the corresponding NIRC*am* filter throughput curves to obtain synthetic fluxes in F115W, F150W, F200W, F277W, F356W, and F444W. Then, for each of the 500 sets of synthetic fluxes per source, we create 1000 realizations of the mock photometry, adding Gaussian noise to the flux in each filter, according to the  $1\sigma$  uncertainties for that source in our photometric catalog. Of those 1000 realizations, we first determine the fraction that would be detected in our *SourceExtractor* run by combining the fluxes and uncertainties in F277W, F356W, and F444W to estimate the SNR in the detection stack, and comparing this to the detection threshold we use in *SourceExtractor*. We then apply our selection cuts to the “detected” mock galaxies to get an estimate of the selection completeness. This way, we obtain 500 values of the selection completeness for each source, corresponding to the 500 draws of  $M_{UV}$ ,  $\beta$ , and  $z$  from the *bagpipes* posterior. Since these completeness values are relatively uncertain, and low values of completeness significantly affect the inferred UVLFs, we cap them at 0.02 to avoid having single objects be weighted by  $> 50\times$ . We discuss this further in Section 4.1.3.

We can then treat the two completeness values independently and obtain a total completeness by multiplying the detection completeness and the selection completeness for each of our sample galaxies, and at each draw from the *bagpipes* posterior. Mathematically, this can be expressed as,

$$C_{\text{tot}}(f_{\text{det}}, M_{UV}, \beta, z) = C_{\text{det}}(f_{\text{det}}) \times C_{\text{sel}}(M_{UV}, \beta, z) \quad (4)$$

where  $f_{\text{det}}$  is the flux in the detection image, and

$$C_{\text{sel}}(M_{UV}, \beta, z) = P(\text{sel} | \text{det}) = \frac{N_{\text{sel} \wedge \text{det}}(M_{UV}, \beta, z)}{N_{\text{det}}(M_{UV}, \beta, z)} \quad (5)$$

where among the 1000 realizations  $N_{\text{det}}$  is the number of mock galaxies that would be detected by **SourceExtractor**, and  $N_{\text{sel} \wedge \text{det}}$  is the number that would be detected and also pass our selection cuts for a given dropout selection.

### 2.9. Binned UV Luminosity Function

Measuring the UVLF means counting galaxies in bins of M<sub>UV</sub> and redshift. In our case, the redshift bins are given by the redshift selection function of each of our dropout samples, characterized as described in the previous Section. We use bins of 1 magnitude in M<sub>UV</sub>, ranging from -22.5 to -18.5 for the F115W dropouts, and replace the three brighter bins by two bins of 1.5 magnitude for the F150W, and the F200W dropouts to account for the smaller number counts in these samples. In each bin, the number density of galaxies is given by

$$\Phi(M_{\text{UV}, \text{bin}}, z_{\text{bin}}) = \sum_{i=0, \dots, N} \frac{1}{V_{\text{eff}, i}} = \sum_{i=0, \dots, N} \frac{1}{C_{\text{tot}, i}(f_{\text{det}, i}, M_{\text{UV}, i}, \beta_i, z_i) V(M_{\text{UV}, \text{bin}})} \quad (6)$$

where the index  $i$  runs over all  $N$  sources in the bin with median UV-magnitude of  $M_{\text{UV}, \text{bin}}$  and median redshift of  $z_{\text{bin}}$ .  $V_{\text{eff}, i}$  is the effective volume over which galaxy  $i$  can be observed and this can be expressed as the total completeness measured for source  $i$  according to equation 4 times the total survey volume  $V$  at  $M_{\text{UV}, \text{bin}}$  which we compute as explained in Section 2.11.

### 2.10. Uncertainties in the UVLF

In order to estimate the total uncertainty in the number density of galaxies in each bin of M<sub>UV</sub>, we need to take into account three independent contributions to the uncertainty: Poisson noise, the effect of measurement uncertainties in M<sub>UV</sub>,  $\beta$ , and  $z$ , and cosmic variance.

#### 2.10.1. Poisson Noise

To estimate the Poisson uncertainty on the number count in a given M<sub>UV</sub> bin, we use the frequentist central confidence interval (see Maxwell 2011). In bins where we count 0 galaxies, we replace  $N$  in Equation 6 by  $N_{\text{ulim}} = 3.8$ , the  $2\sigma$  upper limit for a single-sided Poisson distribution as quoted in Table 1 of Gehrels (1986).

#### 2.10.2. Propagation of Uncertainties in M<sub>UV</sub>, $\beta$ , and $z$

We make use of the Bayesian nature of **bagpipes** and sample 500 SEDs from the posterior distribution from which we measure M<sub>UV</sub>,  $\beta$ , and  $z$  as explained in Section 2.6. This allows us to then generate 500 realizations of the UVLF, applying Equation 6 to each of the 500 values

of  $z$ , M<sub>UV</sub>, and  $\beta$  for each object. The median number densities among these 500 measurements in each M<sub>UV</sub> bin yield our final measurement of the UVLF  $\Phi$ , and the scatter among them quantifies the effect of uncertainties in the photometry, the SED-fitting, and the completeness correction on  $\Phi$ .

#### 2.10.3. Cosmic Variance

Finally, despite the 35 independent lines of sight used in this work, our measurements are subject to cosmic variance. To estimate its contribution to the uncertainty of our UVLFs, we calibrate the cosmic variance to the **UniverseMachine** simulation suite (Behroozi et al. 2019), following Jespersen et al. (2025). This directly incorporates scatter in the stellar-to-halo mass relation as well as possible effects from assembly and environmental biases (Jespersen et al. 2022; Wu et al. 2024; Chuang et al. 2024). We calibrate the cosmic variance in the same bins of M<sub>UV</sub> in which we compute the UVLF as described above, and assuming the  $M_*$ -M<sub>UV</sub> relation from Song et al. (2016). Each field is approximated by a rectangle whose area matches the total area of the field.

To combine the cosmic variance in each magnitude bin across the different fields, we follow the procedure of Valentino et al. (2023),

$$\sigma_{\text{CV}, \text{total}} = \sqrt{\frac{1}{\sum_{\text{fields}} \sigma_{\text{CV}, \text{field}}^{-2}}} \quad (7)$$

where  $\sigma_{\text{CV}, \text{field}}$  is the fractional field-to-field variance in the number count of galaxies. Equation 7 assumes that all fields are independent. Since some PANORAMIC pointings overlap with legacy fields, we add their area to that of the respective legacy field instead of treating them separately. In each bin of M<sub>UV</sub>, we only include fields that are deep enough to contribute sources to that bin, i.e., whose median limiting magnitude (see Section 2.11) is higher than the central value of the M<sub>UV</sub> bin respectively.

The resulting values are included as a contribution to the error bars on our UVLFs by combining the three sources of uncertainty in quadrature as,

$$\sigma_{\Phi}^2 = \sigma_{\text{Poisson}}^2 + \sigma_{\text{phot}}^2 + \sigma_{\text{CV}, \text{total}}^2 \langle N \rangle^2 \quad (8)$$

where  $\sigma_{\text{Poisson}}$  is the Poisson uncertainty,  $\sigma_{\text{phot}}$  is the contribution from uncertainties in the photometry and the SED-fitting, and  $\langle N \rangle$  is the completeness-corrected number count in a given bin of  $z$  and M<sub>UV</sub>.

### 2.11. Survey Area and M<sub>UV</sub> Limits

To account for the varying depth across and between fields used in this work, we measure the survey area

as a function of the  $M_{UV}$  limit up to which we can detect galaxies for each dropout sample. The  $M_{UV}$  limit is given by a combination of the SNR cut in the filter red-wards of the Lyman break in our selection ( $\text{SNR}(\text{FXXXW}) > 8$ ), and the requirement of a color  $> 1.5$  between that filter and the adjacent dropout filter. We start from the weight (“wht”) maps from the DJA, which we combine with the exposure time maps to obtain “full” weight maps, including Poisson noise<sup>4</sup>. Then, we convert those “full” weight maps into rms maps as  $\text{rms} = 1/\sqrt{\text{wht}}$ , and multiply each rms map by a scaling factor that is derived from placing apertures on empty parts of the respective flux map to account for correlated noise (see also Weibel et al. 2024). We then smooth the rms maps with a median filter with a box size of  $7 \times 7$  pixels, roughly corresponding to the area of the circular aperture (radius of 4 pixels) that we use for our photometric catalogs. On the median-filtered rms map, we derive an  $M_{UV}$  limit for each pixel  $i$  as,

$$M_{UV, \text{lim}, i} = 28.9 - 2.5 \log(f_{\text{lim}, i}) - d + 2.5 \log(1 + z_{\text{bin}}) \quad (9)$$

where  $z_{\text{bin}}$  is the median redshift of the respective bin,  $d$  is the distance modulus at  $z_{\text{bin}}$ , and  $f_{\text{lim}, i}$  is defined as,

$$f_{\text{lim}, i} = \text{rms}_i \cdot \sqrt{A_{\text{aper}}} \cdot \text{SNR}_{\text{thresh}} \quad (10)$$

representing the limiting flux at pixel  $i$  where  $\text{rms}_i$  is the rms value at pixel  $i$ , and  $A_{\text{aper}}$  is the area of the circular aperture used to measure the photometry in pixels ( $A_{\text{aper}} = 4^2\pi \approx 50.3$ ). For each redshift bin, we compute two  $M_{UV}$  limit maps: one in the dropout filter, with  $\text{SNR}_{\text{thresh}} = 2$ , and one in the filter red-wards of the break with  $\text{SNR}_{\text{thresh}} = 8$ . The first map specifies the  $M_{UV}$  values corresponding to the  $2\sigma$  upper limit we apply when measuring the Lyman break color. To get the final map of  $M_{UV}$  limits, at each pixel, we add 1.5 to the value in the first map, compare it to the value at the same pixel in the second map, and use the higher value of the two. This is because in order to select a galaxy, the filter red-wards of the break has to be deep enough to *both* detect the galaxy at  $\text{SNR} > 8$ , and measure a color  $> 1.5$  relative to the  $2\sigma$  upper limit in the dropout filter.

We then count the number of pixels whose value of  $M_{UV, \text{lim}, i}$  lies within small bins of  $M_{UV}$  with bin edges given by  $M_{UV, 1}, \dots, M_{UV, j}, M_{UV, j+1}, \dots$  and bin sizes of 0.05 mag. For an  $M_{UV}$  bin used when computing the

UVLF with bin edges  $M_{UV, \text{min}}$  and  $M_{UV, \text{max}}$ , we then obtain the area over which we select galaxies in that bin as,

$$A_{\text{bin}} = \sum_{j: M_{UV, j} > M_{UV, \text{min}}} g(M_{UV, j}) \sum_i f_i(M_{UV, j}) \quad (11)$$

where

$$f_i(M_{UV, j}) = \begin{cases} 1 & \text{if } M_{UV, j-1} < M_{UV, \text{lim}, i} < M_{UV, j} \\ 0 & \text{else} \end{cases} \quad (12)$$

determines if pixel  $i$  lies in the small 0.05 mag  $M_{UV}$  bin  $j$ , and

$$g(M_{UV, j}) = \begin{cases} \frac{M_{UV, j} - M_{UV, \text{min}}}{M_{UV, \text{max}} - M_{UV, \text{min}}} & \text{if } M_{UV, j} < M_{UV, \text{max}} \\ 1 & \text{else} \end{cases} \quad (13)$$

measures the fraction of the UVLF bin ( $M_{UV, \text{min}}, M_{UV, \text{max}}$ ) between  $M_{UV, \text{min}}$  and the upper edge  $M_{UV, j}$  of the smaller bin ( $M_{UV, j-1}, M_{UV, j}$ ).

We note that in practice, a galaxy in our sample with e.g., a measured  $M_{UV} = -19$  is not guaranteed to be observed in a part of the mosaic with a nominal  $M_{UV}$  limit  $> -19$  due to the noise in the data that can up-scatter fainter galaxies above our selection threshold. This is, however, accounted for in our completeness correction, and the area computed as described above provides a more accurate estimate of the true area over which galaxies are selected compared to approaches determining an  $M_{UV}$  limit per field.

We slightly simplify this procedure for the Abell-2744 cluster field where we measure the median  $M_{UV}$  limit and then assume this to be constant across the field. Using the strong lensing model described in Section 2.7, we can then compute the area above a given  $M_{UV}$  limit as the area with a magnification larger than what is required to reach the respective depth. Note that this is done directly in the source plane in order to obtain the volume effectively probed with the available observations.

## 2.12. Fitting the UVLF

We fit two parametric curves to the obtained UVLFs, a single Schechter function, and a double power-law (DPL).

These functions can be described as,

<sup>4</sup> <https://dawn-cph.github.io/dja/blog/2023/07/18/image-data-products/>

$$\Phi_{\text{Schechter}}(M_{\text{UV}}) = 0.4 \ln(10) \Phi^* 10^{-0.4(M_{\text{UV}} - M_{\text{UV}}^*)(\alpha+1)} \times \exp(-10^{-0.4(M_{\text{UV}} - M_{\text{UV}}^*)}) \quad (14)$$

and

$$\Phi_{\text{DPL}} = \frac{\Phi^*}{10^{-0.4(M_{\text{UV}} - M_{\text{UV}}^*)(\alpha+1)} + 10^{-0.4(M_{\text{UV}} - M_{\text{UV}}^*)(\beta+1)}} \quad (15)$$

To account for Eddington bias introduced by the uncertainties in  $M_{\text{UV}}$ , we convolve the fitting functions with a Gaussian before fitting, i.e., we fit the function

$$\Phi_{\text{conv}}(M_{\text{UV}}) = \int_{-\infty}^{\infty} \Phi_{\text{param}}(x) G(M_{\text{UV}} - x) dx \quad (16)$$

to the observed UVLF where  $G$  is a Gaussian whose width is given by the median  $1\sigma$  uncertainty in  $M_{\text{UV}}$  in each dropout sample, and  $\Phi_{\text{param}}$  stands for  $\Phi_{\text{Schechter}}$  and  $\Phi_{\text{DPL}}$  respectively.

We perform the fitting to each of the 500 UVLFs sampled from the **bagpipes** posterior, and use the median, as well as the 16th and 84th percentiles of the derived fitting parameters as our final estimates and their uncertainties.

Since we cannot fit for all the parameters simultaneously at  $z \sim 13$  and  $z \sim 17$  (see Section 3.3), we also adopt the DPL parametrization from [Donnan et al. \(2024\)](#) to determine the values of  $M_{\text{UV}}^*$ ,  $\alpha$  and  $\beta$  at the median redshift of our samples respectively, and only fit for the normalization  $\Phi^*$ .

### 3. RESULTS

#### 3.1. High-Redshift Candidates

Subsequently, we discuss our three samples, mentioning some sources that have already been published, as well as highlighting the most compelling new candidates identified in this work.

##### 3.1.1. $z \sim 10$ Sample

Spectroscopically confirmed sources in our  $z \sim 10$  sample include two sources in the EGS from [Arrabal Haro et al. \(2023\)](#), and three sources in the A2744 cluster field from [Napolitano et al. \(2025\)](#), as well as GN-z11 ([Oesch et al. 2016](#); [Bunker et al. 2023](#)). We further selected two galaxies that were first mentioned as  $z \sim 9 - 10$  candidates (in addition to GN-z11) in [Oesch et al. \(2014\)](#) namely their GN-z10-2, and GN-z9-1.

In Figure 3, we highlight four new candidates. The source in the top left is a robust  $z \sim 10$  galaxy candidate in the UDS field which shows a sharp rise in the SED around the Balmer break as probed by both the F444W and the F410M filter. The best-fitting SED

therefore prefers a solution with a low star formation rate (SFR) in the last  $\sim 10$  Myr, reminiscent of so-called napping or “mini-quenched” galaxies that have been observed at slightly lower redshifts (e.g., [Strait et al. 2023](#); [Looser et al. 2024](#)). The source is also detected in MIRI/F770W, which suggests a further rising SED, inconsistent at the  $\sim 2\sigma$ -level with the supposed absence of strong H $\alpha$ -emission. Together with the point-source like morphology, this could indicate the presence of an AGN boosting the rest-optical continuum or contributing to the H $\alpha$  flux. The photometry suggests a V-shaped SED with a Balmer Break as is observed for so-called Little Red Dots (e.g. [Matthee et al. 2024](#); [Akins et al. 2024](#); [Kokorev et al. 2024b](#); [Labbe et al. 2025](#); [Greene et al. 2024](#); [Kocevski et al. 2024](#); [Wang et al. 2024](#); [Ji et al. 2025](#)), of which the most distant known so far is CAPERS-LRD-z9 at  $z_{\text{spec}} = 9.28$  ([Taylor et al. 2025](#)). A similar but fainter source is shown in the top right. This source lies in the GOODS-S and was imaged in one of the deepest PANORAMIC images ( $\sim 27$  hours total integration). Again, the excess in both F444W and F410M and the flat color between them suggests the presence of a (small) Balmer break which may reflect a current off-mode of star formation in this galaxy at  $z \sim 9.7$ .

The two sources in the bottom are two of the most striking candidates identified in PANORAMIC imaging outside of any legacy fields. They are both located in the same pointing (J013748M2152), at a physical separation of only 81 proper kpc, and their photometric redshifts are consistent with each other. Again, similar to the two sources in the top panels, ID 9329 shows hints of a Balmer break as traced by F410M and F444W. While difficult to disentangle from line emission, a tentative Balmer break is observed in  $> 10\%$  of all galaxies in the F115W dropout sample. If confirmed, this suggests that LRD-type AGN are quite numerous out to  $z \sim 10$ , or that bursty star formation is common at  $z \sim 10$ , even at relatively high masses (up to  $M_* \sim 10^9 M_{\odot}$  as indicated by our **bagpipes** fits).

##### 3.1.2. $z \sim 13$ Sample

Our  $z \sim 13$  sample contains 3 objects with spectroscopic redshifts: GHZ2/GLASS-z12 ([Castellano et al. 2024](#)), GS-z12-0 from [Curtis-Lake et al. \(2023\)](#), and JADES-GS-z14-0 from [Carniani et al. \(2024a\)](#).

We show two promising  $z \sim 14$  candidates identified from PANORAMIC imaging in Figure 4. ID 35840, initially discovered by McLeod et al. (in prep.), shows a blue UV-continuum, and a clear break between F200W and F150W (a factor of 6, or 2 mag, with a  $2\sigma$  upper limit in F150W). The slight drop in F200W indicates



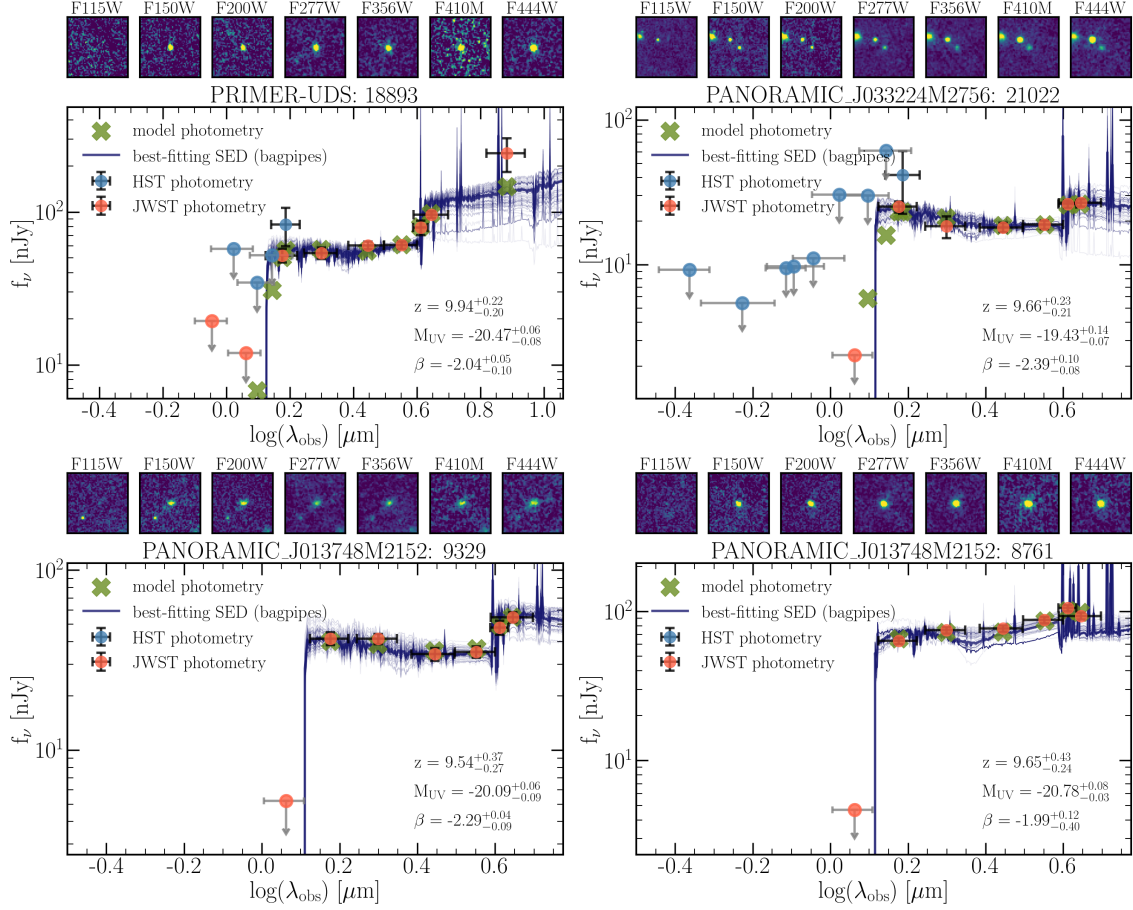


**Figure 3.** Some of the most intriguing new  $z \sim 10$  candidates identified as F115W dropouts in this work. Top left: A galaxy in the UDS with a possible Balmer break at  $z \sim 9.94$ , and a MIRI/F770W detection hinting at a rising SED in the rest-frame optical, creating a V-shape, reminiscent of Little Red Dots. Top right: A fainter robust candidate in the GOODS-S field with deep imaging from PANORAMIC, also showing signs of a Balmer Break. Bottom: Two bright candidates from PANORAMIC imaging outside legacy fields. Both are found in the same pointing, at a physical separation of only 81 kpc and with consistent photometric redshifts. The thin blue lines show 100 samples of the best-fitting SED from the *bagpipes* posterior respectively.

that the Lyman break is inside that filter, setting the photometric redshift to  $z \sim 14.5$ . If confirmed, this source may break the current redshift record ( $z_{\text{spec}} = 14.44$ , [Naidu et al. 2025](#)), but at a UV-luminosity of  $M_{\text{UV}} \sim -21.2$ , similar to JADES-GS-z-14-0 ([Carniani et al. 2024a](#)). NIRSpec follow-up of the source is scheduled in cycle 4 through the GO program 6954 (PIs Donnan & McLeod). The source with ID 3640 on the right is identified in significantly shallower imaging ( $5\sigma$  depth in F200W of 27.8 mag, compared to 29.3 mag in the J221700P0025 pointing in which ID 35840 is found), but nevertheless shows a break strength of 1.54 mag between F200W and F150W because it is even more luminous at  $M_{\text{UV}} \sim -21.7$  making it the most luminous galaxy in our F150W dropout sample.

### 3.1.3. $z \sim 17$ Sample

We discuss the four F200W dropouts that passed our selection cuts below and conclude that none of them is a plausible  $z \sim 17$  candidate. First, we select the interloper known as the Schrödinger galaxy ([Naidu et al. 2022a](#); [Harikane et al. 2023](#); [Donnan et al. 2023](#); [Arrabal Haro et al. 2023](#)). Then, we identify an extremely promising candidate in the A2744 cluster field with a plausible blue UV continuum and a sharp break between F277W and F200W, indicating a redshift of  $\sim 18$  at  $M_{\text{UV}} \sim -20.1$ . However, as has been discussed in [Castellano et al. \(2025\)](#), this source turns out to be a transient. It was completely absent from epoch 1 imaging by GLASS in June 2022, and only showed up in epoch 2 imaging in November 2022, where unfortunately it fell into the chip gap of the NIRCcam/SW detector and thus created a fake SW dropout source when imaging from both epochs is combined.

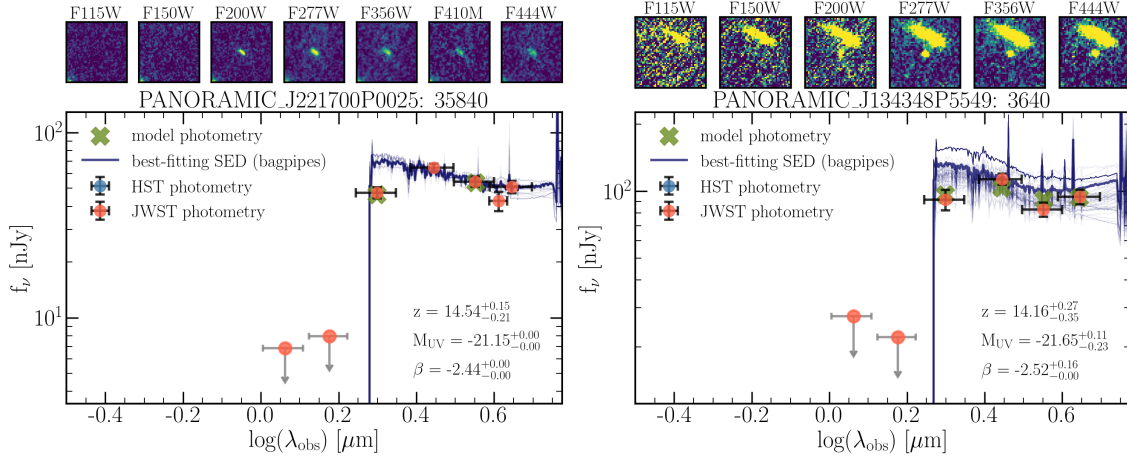


**Figure 4.** Same as Figure 3 with the most promising  $z \gtrsim 13$  candidates from PANORAMIC, identified as F150W dropouts. If confirmed, the source on the left (McLeod et al. in prep.) could break the current redshift record (Naidu et al. 2025) with a UV-luminosity similar to JADES-GS-z-14-0 (Carniani et al. 2024a). ID 3640 on the right shows a slightly lower photometric redshift, but, if confirmed, is even more luminous at  $M_{UV} \sim -21.7$ .

The third  $z \sim 17$  candidate we select lies in the UDS field and is shown in Figure 5. Its photometry, if it were at  $z \sim 17$ , indicates a blue UV-continuum ( $\beta = -2.29 \pm 0.26$ ). It lies next to a brighter source that also becomes fainter at shorter wavelengths probed by JWST/NIRCam, and that has a photometric redshift of  $z_{\text{phot}} = 4.85 \pm 0.19$ . Indeed, our candidate has a spectrum from CAPERS which reveals the [O III], H $\beta$ , and H $\alpha$  lines lining up to boost the flux of all the LW filters, including F410M, and unambiguously putting the source at  $z_{\text{spec}} = 4.9$ , identical to the Schrödinger galaxy.

Our last F200W dropout candidate lies in a relatively crowded part of the UDS field. It shows an extended morphology and a low surface brightness which seems atypical of high redshift galaxies. More importantly, as many as four immediate neighbors of the source have photometric redshifts consistent within  $1\sigma$  with a redshift  $< 0.3$  different from the notorious  $z \sim 4.9$  which is also the preferred solution identified by *eazy* for the source itself. We therefore argue that this source is likely not at  $z \sim 17$ . An RGB imaging cutout of the source and its surroundings, with potential neighboring galaxies labeled with their photometric redshifts is shown in Figure 6.

When computing the UVLF below, we assume that we did not identify any plausible  $z \sim 17$  galaxies and only show upper limits on the number density at that redshift.

### 3.2. UV Luminosity Functions

We present the UVLFs measured for our three dropout samples, corresponding to redshifts of  $z \sim 10$ ,  $z \sim 13$ , and  $z \sim 17$  in Figure 7. All our measured val-

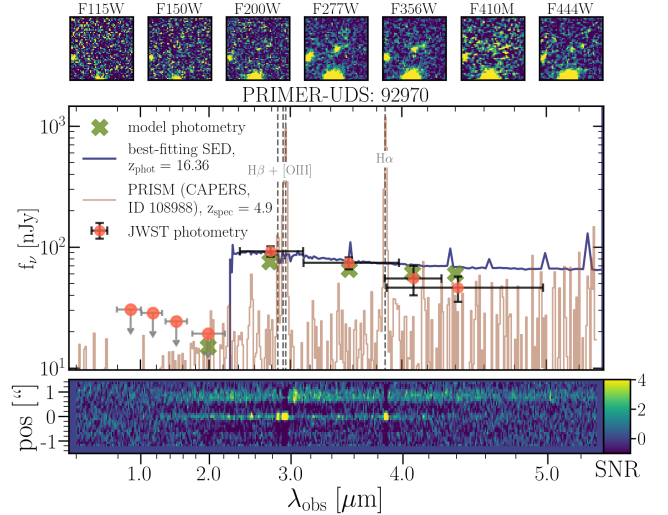


**Figure 5.** One of our F200W dropout candidates with its NIRSpect/PRISM spectrum from CAPERS revealing the [O III], H $\beta$ , and H $\alpha$  emission lines which boost all four LW filters (F277W, F356W, F410M, and F444W) at  $z_{\text{spec}} = 4.9$ . The 1D spectrum is shown as the brown line, and the SNR of the 2D spectrum is shown in the bottom panel to better illustrate the clear emission line detections.

ues and uncertainties are listed in Table 1. There are two panels for each dropout sample in Figure 7, both showing our UVLF and best-fitting DPL curve (adopting the parametrization from Donnan et al. (2024), and only fitting for  $\Phi^*$ ) with uncertainties. The  $M_{UV}$  values at which the points are plotted are given by the median  $M_{UV}$  of the sample galaxies in a given bin. In the left panels, we compare to observational results from Bouwens et al. (2021), Harikane et al. (2023), Pérez-González et al. (2023), Leung et al. (2023), McLeod

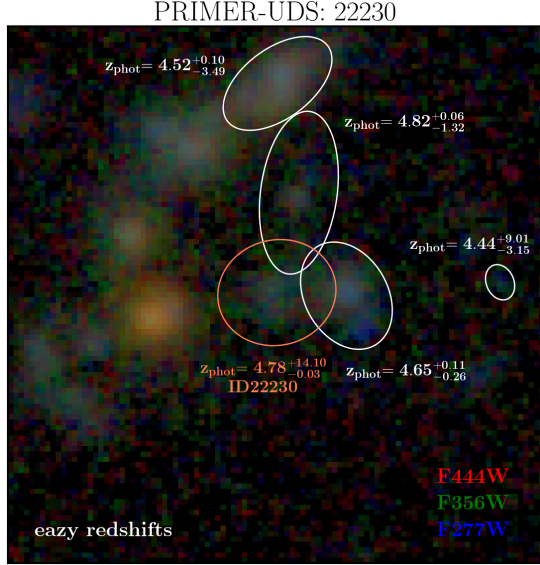


**Figure 6.**  $4.04'' \times 4.04''$  RGB imaging cutout of one of our F200W dropout  $z \sim 17$  candidates and its surroundings, highlighting sources with photometric redshifts consistent with  $z = 4.9$ , where at least two interlopers contaminating  $z \sim 17$  F200W dropout searches are known.

et al. (2024), Harikane et al. (2024), Adams et al. (2024), Willott et al. (2024), Finkelstein et al. (2024), Robertson et al. (2024), Donnan et al. (2024), Rojas-Ruiz et al. (2024), Kokorev et al. (2024a), Morishita et al. (2025), Whitler et al. (2025), Adams et al. (2025), Pérez-González et al. (2025), and Castellano et al. (2025).

The blue dots in the upper left and middle left panels represent number density estimates based on PANORAMIC data only. For this comparison, we only include the 30 PANORAMIC pointings outside of any legacy imaging. The measurements are plotted 0.2 magnitudes lower in  $M_{UV}$  for better visual separation. They are all consistent within error bars with the measurements including all fields, illustrating the power of pure parallel imaging in only 6 NIRCcam filters to provide an unbiased view of the galaxy population at  $z \gtrsim 9$ . In the F150W dropout sample, there are only two PANORAMIC candidates outside of any legacy fields which are both shown in Figure 4, and yield the number density shown as a blue point at the bright end of the UVLF in the middle left panel. This is consistent with, but slightly higher than the measurement from the full data set. As discussed in Section 3.1.2, while we argue that the candidate with ID 35840 is robust, the supposedly even brighter candidate with ID 3640 is identified in shallower imaging and leaves more room for a low- $z$  solution. If we remove this object from the sample, the resulting number density in the brightest bin at  $z \sim 12.7$  drops to  $\log(\Phi/\text{Mpc}^{-3}\text{mag}^{-1}) = -6.38^{+0.27}_{-0.82}$  for the full

sample, and to  $\log(\Phi/\text{Mpc}^{-3}\text{mag}^{-1}) = -5.98^{+0.31}_{-\infty}$  for the PANORAMIC data only.

Splitting the uncertainties on our measured number densities in the three components specified in Equation 8, we find that cosmic variance dominates the error in the brightest bin at  $z \sim 10$ , followed by the Poisson uncertainty. In fainter bins,  $\sigma_{\text{phot}}$  starts to dominate due to the uncertainty in the completeness correction, followed by  $\sigma_{\text{CV}}$  while  $\sigma_{\text{Poisson}}$  becomes negligible. At  $z \sim 13$ , the upper error bar (i.e., the difference between the 84th percentile and the median) is always dominated by  $\sigma_{\text{phot}}$ , driven by uncertainties in the completeness correction. In the faintest bin,  $\sigma_{\text{phot}}$  also dominates the lower error bar, but in the two brighter bins,  $\sigma_{\text{CV}}$  followed by  $\sigma_{\text{Poisson}}$  have a stronger effect on the lower error bar.

From our F115W dropout sample at a median redshift of  $z \sim 9.7$ , we measure a UVLF that is consistent with most literature results at comparable redshifts. Our measured number density in the brightest  $M_{UV}$  bin has more constraining power than other literature results thanks to the large area probed and the many independent lines of sight, and confirms the large abundance of bright galaxies at  $z \sim 10$ , suggesting a shallow slope at the bright end of the UVLF out to  $M_{UV} \sim -22$  (see Section 3.3).

At  $z \sim 12.7$ , the median redshift of our F150W dropout sample, our measurements lie somewhat below published results. In the brightest bin, at  $M_{UV} \sim -21$ , our data point is consistent within  $1\sigma$  with Donnan et al. (2024), who measured the UVLF at  $z \sim 12.5$ , while in the faintest bin ( $M_{UV} \sim -19$ ), our measurement is consistent with all displayed results due to the large uncertainty driven by  $\sigma_{\text{phot}}$  discussed above. At intermediate UV luminosities ( $M_{UV} \sim -20$ ), however, we find relatively few galaxies, resulting in  $> 1\sigma$  discrepancies with most literature results at similar redshifts, and also below the lower limit inferred by Harikane et al. (2024) from a pure spectroscopic sample at  $z \sim 12$ . This then suggests a somewhat faster decrease in the overall number density of galaxies from  $z \sim 10 - 13$  compared to most literature results, as we will further explore below.

Moving to our highest redshift bin, our upper limits at  $z \sim 17$  are more constraining than previously published upper limits thanks to the larger survey area probed here. At  $M_{UV} \sim -19$ , our upper limit coincides with the measurement of Pérez-González et al. (2025) and the parametrization from Donnan et al. (2024). We do not probe faint enough magnitudes to directly compare to the fainter bins from Pérez-González et al. (2025), or Kokorev et al. (2024a), but our fit to the upper limits, extrapolated to fainter magnitudes with the Donnan et al. (2024) parametrization suggests lower number den-

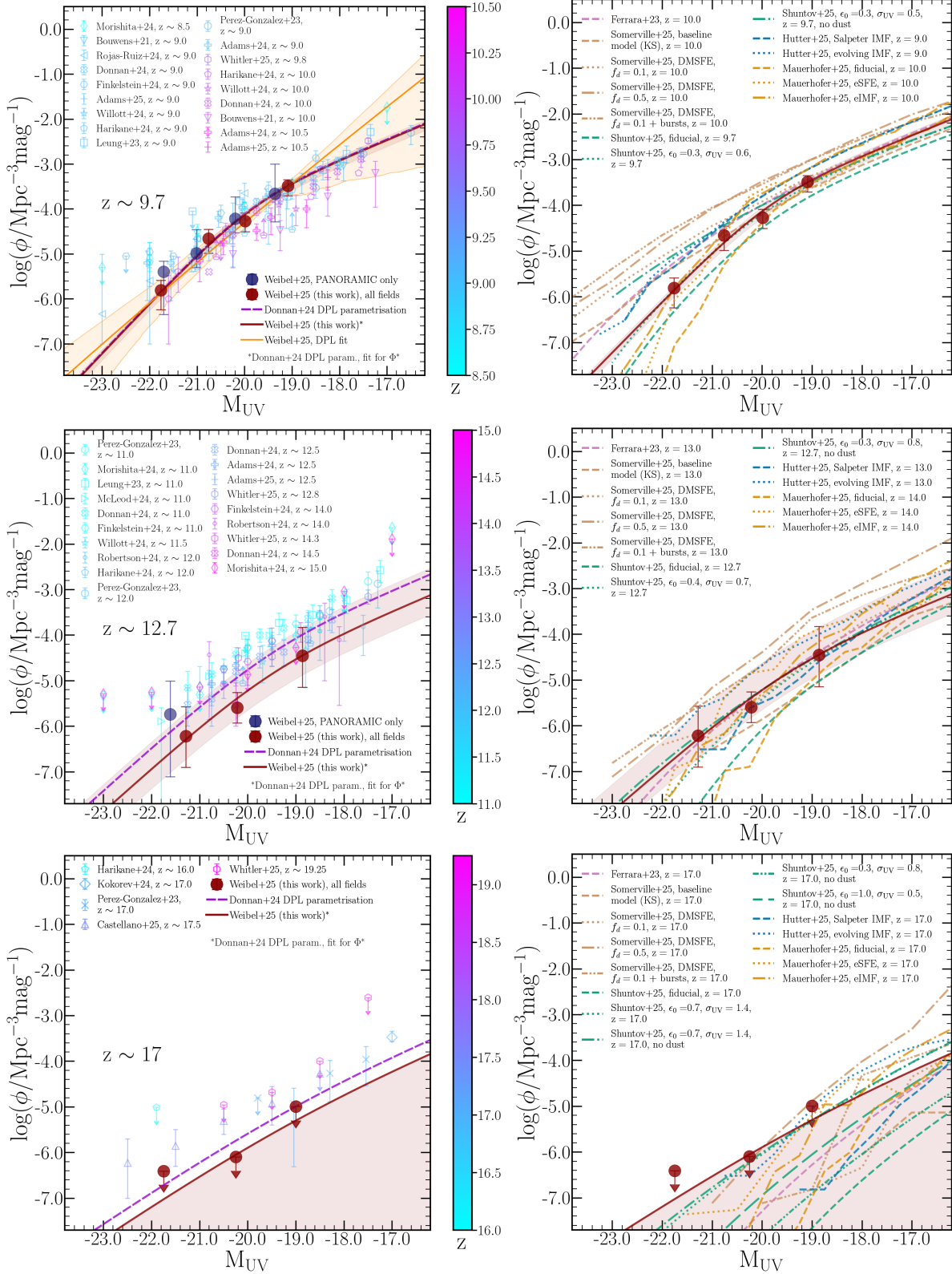


**Figure 7.** Binned UVLFs inferred from our F115W (top), F150W (middle), and F200W (bottom) dropout samples. Number densities inferred from our full sample are shown as red dots, and those from PANORAMIC data only as blue dots. The red solid lines and shaded regions indicate our best-fitting DPL curve, where we adopted the parametrization from [Donnan et al. \(2024\)](#) (dark violet dashed lines in the left panels), and only fit for the normalization  $\Phi^*$ . In the top left panel (F115W dropouts) we further show our best-fitting DPL function where we fit for all parameters simultaneously. We compare to observational results on the left, and to models and simulations on the right, as indicated in the Figure legends and discussed in the text. Observational results are color-coded by their redshift within the redshift range covered by each panel.



**Table 1.** Measured UVLF-values from the three dropout samples, corresponding to  $z \sim 10$ , 13 and 17.

Redshift bin	$M_{UV}$	$\log(\Phi/\text{Mpc}^{-3} \text{ mag}^{-1})$
$z \sim 10$	-21.76	$-5.81^{+0.22}_{-0.43}$
	-20.76	$-4.66^{+0.21}_{-0.32}$
	-19.99	$-4.27^{+0.18}_{-0.24}$
	-19.09	$-3.49^{+0.14}_{-0.22}$
$z \sim 13$	-21.28	$-6.22^{+0.65}_{-0.68}$
	-20.22	$-5.59^{+0.33}_{-0.33}$
	-18.86	$-4.45^{+0.62}_{-0.70}$
$z \sim 17$	-21.75	$< -6.40$
	-20.25	$< -6.10$
	-19.00	$< -5.00$

sities than their measurements. As discussed in [Kokorev et al. \(2024a\)](#), if their number density is correct, a steep faint-end slope of the UVLF is required to match both their measurement and our upper limit at  $M_{UV} \sim -19$ . At  $M_{UV} \sim -20$ , our  $2\sigma$  upper limit lies slightly below the DPL parametrization by [Donnan et al. \(2024\)](#), and the measurements from [Castellano et al. \(2025\)](#) who however also specify upper limits at roughly the same number densities as their measurements, reflecting the case where their candidates turn out to be low redshift interlopers.

### 3.3. Best-Fitting Parametric Functions

As described in Section 2.12, we follow three different fitting approaches: Fitting a Schechter function, a DPL, and adopting the DPL parametrization from [Donnan et al. \(2024\)](#), and only fitting for the normalization  $\Phi^*$ . We start with the Schechter fit at  $z \sim 10$ , leaving all parameters unconstrained. In this case, of the 500 fits to the UVLF sampled from the **bagpipes** posterior, the majority prefers a solution with an extremely low normalization ( $\log(\Phi_{\text{Schechter}}^*) < -14$ ), and pushing  $M_{UV, \text{Schechter}}^*$  out to  $< -30$ , making the fitted curve look like a single power law with a slope of  $\sim -3$ . If we instead directly fit to the data points and their errors shown in Figure 7, we find a decent fit with  $\log(\Phi_{\text{Schechter}}^*) = -5.49$ ,  $M_{UV, \text{Schechter}}^* = -21.91$ , and  $\alpha_{\text{DPL}} = -2.81$ . The low normalization and high  $M_{UV}^*$  illustrate that our measured UVLF at  $z \sim 10$  is not well described by a Schechter function because it does not show an exponential cut-off at the magnitudes probed here. We therefore proceed with the DPL fit and

find  $\log(\Phi_{\text{DPL}}^*) = -4.01^{+0.10}_{-0.20}$ ,  $M_{UV, \text{DPL}}^* = -20.0^{+0.11}_{-0.42}$ ,  $\alpha_{\text{DPL}} = -2.98^{+0.84}_{-0.60}$ , and  $\beta_{\text{DPL}} = -3.38^{+0.53}_{-0.68}$ . Both the bright and especially the faint end slope of the UVLF are poorly constrained in this fit due to the limited constraining power of the data. Adopting the DPL parametrization proposed by [Donnan et al. \(2024\)](#) as  $M_{UV, \text{D}+24}^*(z = 9.7) = -19.88$ ,  $\alpha_{\text{D}+24}(z = 9.7) = -2.1$ , and  $\beta_{\text{D}+24}(z = 9.7) = -3.79$ , we fit for the normalization and obtain  $\log(\Phi_{\text{D}+24-\text{fit}}^*)(z = 9.7) = -3.74^{+0.09}_{-0.14}$ , almost identical to their value of  $\log(\Phi_{\text{D}+24}^*) = -3.72$ . At  $z \sim 13$ , the constraining power of our data is not sufficient to fit for all parameters of either the Schechter or the DPL curve simultaneously. We therefore only follow the third approach and find  $\log(\Phi_{\text{D}+24-\text{fit}}^*)(z = 12.7) = -4.59^{+0.60}_{-0.43}$ , significantly lower than the parametrization from [Donnan et al. \(2024\)](#) which gives  $\log(\Phi_{\text{D}+24}^*)(z = 12.7) = -4.14$ . Finally, at  $z \sim 17$ , we perform the same fit only to our most constraining upper limit at  $M_{UV} \sim -20.25$  to get an upper limit on the normalization of  $\log(\Phi_{\text{D}+24-\text{fit}}^*)(z \sim 17) < -5.05$ , again lower than the [Donnan et al. \(2024\)](#) parametrization,  $\log(\Phi_{\text{D}+24}^*)(z = 17) = -4.74$ .

We show our fitted curves following the last approach, and the DPL fit at  $z \sim 10$  in Figure 7, with the shaded regions highlighting the range between the 16th and 84th percentile of the fits to the 500 realizations of the UVLFs sampled from the **bagpipes** posterior.

### 3.4. Comparing to Modeled UVLFs

In the following, we compare our measurements to various theoretical models. Using the modeling framework from [Shuntov et al. \(2025\)](#), we first explore how changes to parameters tracing the star formation efficiency (SFE) and the burstiness of star formation can match our measured UVLFs. Then, we compare to models from the literature that implement changes to the IMF or the SFE at high redshift in a physically motivated way ([Hutter et al. 2025](#); [Mauerhofer et al. 2025](#); [Somerville et al. 2025](#)), and to a simple physical model without dust attenuation ([Ferrara et al. 2023](#)).

#### 3.4.1. The Shuntov et al. (2025) Framework

In short, the [Shuntov et al. \(2025\)](#) modeling framework is based on an instantaneous star formation efficiency (SFE) that relates the SFR to the halo mass accretion rate. The SFR is then converted to an  $M_{UV}$  assuming a conversion factor  $\kappa_{UV}$  from [Madau & Dickinson \(2014\)](#) which is degenerate with  $\epsilon_0$ , the normalization of the SFE. The [Shuntov et al. \(2025\)](#) framework assumes empirical relations for  $A_V - \beta$  ([Meurer et al. 1999](#)) and  $\beta - M_{UV}$  ([Bouwens et al. 2014](#)) to model dust, and adds Gaussian scatter to the  $M_h - M_{UV}$  relation,

described by the parameter  $\sigma_{UV}$ . They combine this with a model of the halo occupation distribution (HOD) to simultaneously model both the UVLF and the two-point correlation function (2PCF), and constrain the model parameters (i.e., the parametric form of  $\epsilon_0$ ,  $\sigma_{UV}$  and the HOD) from UVLF and 2PCF measurements based on spectroscopic samples of [O III] and H $\alpha$  emitters from FRESCO (Oesch et al. 2023) and CONGRESS at  $z \sim 4.3$ ,  $z \sim 5.4$ , and  $z \sim 7.3$ . Fixing the model parameters at the values constrained at  $z = 8$ , they then extrapolate the UVLF to higher redshifts, essentially following the evolution of the halo mass function from Watson et al. (2013).

In Figure 7, we present their fiducial model with peak efficiency  $\epsilon_0 = 0.23$  and scatter  $\sigma_{UV} = 0.5$ , as well as other models that illustrate the impact of different parameters on the UVLF. At  $z \sim 10$ , the fiducial model only lies slightly below our measurements. Increasing the scatter to  $\sigma_{UV} = 0.6$ , and the efficiency to  $\epsilon_0 = 0.35$  provides a decent fit to the data. To demonstrate the impact of dust on the UVLF, we show another model with  $\sigma_{UV} = 0.5$  and  $\epsilon_0 = 0.3$ , but with no dust attenuation. This model overshoots at the bright end of the UVLF, emphasizing that in this framework, dust still plays an important role for the brightest galaxies at  $z \sim 10$ .

To match our measured UVLF at  $z \sim 13$ , we further increase both parameters to  $\epsilon_0 = 0.4$  and  $\sigma_{UV} = 0.7$ . Alternatively, a smaller peak efficiency  $\epsilon_0 = 0.3$  and  $\sigma_{UV} = 0.8$  with no dust attenuation produces a remarkably good fit to the data, illustrating the degeneracy between these different parameters in boosting the UVLF. While we cannot break these degeneracies, we emphasize that modest tweaks to the fiducial model are sufficient to reproduce our UVLF at  $z \sim 13$ .

In our highest redshift bin, at  $z \sim 17$ , we show four models in addition to the fiducial one: (1) a “maximum” model that is just consistent with our upper limits,  $\epsilon_0 = 0.7$ , and  $\sigma_{UV} = 1.4$ , (2) the same without dust attenuation, which only has a minor impact at  $z \sim 17$ , (3) one of the models shown to match the data at  $z \sim 13$  ( $\epsilon_0 = 0.3$  and  $\sigma_{UV} = 0.8$  without dust), and (4) a model with maximum efficiency and smaller UV-scatter ( $\epsilon_0 = 1.0$ ,  $\sigma_{UV} = 0.5$ , no dust). The latter two lie well below our upper limits. A further increase in  $\epsilon_0$  and/or  $\sigma_{UV}$  with redshift at  $\gtrsim 13$  is thus allowed by the data, but not required.

### 3.4.2. Other Models from the Literature

Motivated by local observations of a more top-heavy IMF in regions with higher SFR (e.g. Jeřábková et al. 2018), and the idea that denser gas regions are more likely to form massive stars, Hutter et al. (2025) model

an IMF that becomes more top-heavy with increasing specific SFR (sSFR) above a redshift-dependent threshold in sSFR. The curves shown in Figure 7 represent two models: one with a Salpeter IMF, and one with their evolving IMF. Both models lie slightly above our measurements at  $z \sim 10$ , where they produce very similar UVLFs. At  $z \sim 13$ , their two models differ more significantly. Interestingly, the model based on a Salpeter IMF is consistent with the data, while the evolving IMF model lies above our measurement at  $M_{UV} \sim -20$ . Both models are consistent with our upper limits at  $z \sim 17$ , with the evolving IMF model being close to our  $2\sigma$  upper limit at  $M_{UV} \sim -20$ . The relatively rapid evolution in the UVLF from  $z \sim 10$ – $17$  we see in the data is therefore more consistent with their Salpeter IMF model, than their evolving IMF scenario.

We further show models from Mauerhofer et al. (2025) who implement interstellar medium physics from SPHINX<sup>20</sup> (Rosdahl et al. 2022) into the DELPHI semi-analytical model (Dayal et al. 2014). We show their fiducial model, one where they implement an increasing SFE with redshift (eSFE), and one with an evolving IMF (eIMF) that becomes more top-heavy at lower metallicity and higher redshift. Their fiducial model lies below our measured UVLFs at the bright end at  $z \sim 10$ , and  $z \sim 13$ , meaning that a boost to these modeled UVLFs is required to match the data. Indeed, both the eSFE and the eIMF models provide better fits at  $z \sim 10$ , with the eIMF being slightly too high at the faint end. The eIMF model agrees with our data points at  $z \sim 13$  within error bars, while the eSFE model lies above our constraints at  $M_{UV} \sim -20$ . At  $z \sim 17$ , all their models are consistent with our constraints, with both the eIMF, and the eSFE models being close to our upper limit at  $M_{UV} \sim -19$  due to their steepness. None of their models therefore consistently reproduces our measured UVLFs across the redshift and magnitude range explored here. While their eSFE and eIMF models match the measured number density in the brightest bins of the UVLF at  $z \sim 10$ – $13$ , they tend to produce too many galaxies at fainter magnitudes, and possibly at  $z \gtrsim 15$ .

Next, we compare to models from Somerville et al. (2025) who implement a scaling of the SFE with the gas surface density into the Santa Cruz semi-analytical model (Somerville & Primack 1999; Somerville et al. 2001). This model is labeled as density-modulated star formation efficiency (DMSFE). We show their baseline model, two versions of the DMSFE model with different fractions of the ISM in dense star forming clouds ( $f_d = 0.1$ , and  $f_d = 0.5$ ), and the DSFME model with  $f_d = 0.1$  and additional bursts in star formation added in post-processing. At  $z \sim 10$ , their baseline model is

consistent with our measurements down to  $M_{UV} \sim -21$ , but produces higher number densities in the brightest bin ( $M_{UV} \sim -22$ ). All other models produce even higher UVLFs. Note that the models shown here are not corrected for dust attenuation, whose impact is however limited (see e.g., Figure 10 in Somerville et al. 2025). At  $z \sim 13$ , their baseline model lies slightly below the data at  $M_{UV} \sim -20$ , while the DMSFE with  $f_d = 0.1$  provides a good fit across the entire magnitude range. The other two modeled UVLFs ( $f_d = 0.5$ , and  $f_d = 0.1$  with additional bursty star formation) still lie above our measurements. The baseline and the  $f_d = 0.1$  models lie below our upper limits at  $z \sim 17$ , where the  $f_d = 0.5$  model lies slightly above our upper limit at  $M_{UV} \sim -19$ . Consistent with the models explored previously, this indicates that only a modest change to the fiducial models (in this case, an ISM fraction in dense clouds of 10%) is needed to account for the number density of UV-bright galaxies at  $z \sim 13$ , and substantially more significant changes to the baseline model are disfavored by both our measured UVLF at  $z \sim 13$  and the upper limits at  $z \sim 17$ .

Finally, we compare to the attenuation free model (AFM) from Ferrara et al. (2023) who explore a minimal physical model where high redshift galaxies are not attenuated by dust. This could be due to efficient feedback-driven ejection of dust in early galaxies. At  $z \sim 10$ , their model produces slightly higher number densities at the bright end compared to our measurements, but it provides a good fit at  $z \sim 13$ , and lies well below our upper limits at  $z \sim 17$ . In the context of this simple model, the slightly lower number densities we measure at the bright end at  $z \sim 10$  may be related to non-negligible dust attenuation affecting the brightest galaxies at those epochs, as also suggested by our modeling based on the framework from Shuntov et al. (2025).

### 3.5. UV Luminosity and Star Formation Rate Density

We integrate our fitted parametric curves in the range  $M_{UV} \in (-23, -17)$  to calculate the cosmic UV-luminosity density  $\rho_{UV}$ , and show it in Figure 8. To estimate uncertainties, we integrate the curves fitted to the 500 realizations of our UVLFs, and show the median, 16th and 84th percentile of the resulting 500 values of  $\rho_{UV}$  as our measurement and error bar respectively.

Adopting the conversion factor from Madau & Dickinson (2014),  $\kappa_{UV} = 1.15 \times 10^{-28} M_{\odot} \text{ yr}^{-1} / (\text{erg s}^{-1} \text{ Hz}^{-1})$ , we show the cosmic star formation rate density (cSFRD) on the secondary y-axis on the right of Figure 8. We compare to JWST-based literature results from McLeod et al. (2024); Harikane et al. (2024); Willott

et al. (2024); Finkelstein et al. (2024); Whitler et al. (2025), and Pérez-González et al. (2025), as well as to a subset of the models displayed on the right of Figure 7, where we consistently integrate the modeled UVLFs in the range  $M_{UV} \in (-23, -17)$  to enable a direct comparison to the data. We further show a pre-JWST parametrization and its extrapolation to  $z > 9$  from Bouwens et al. (2021), and the parametrization from Donnan et al. (2024).

As expected, at  $z \sim 10$ , our measurements are consistent with the displayed JWST-based literature results. The values and error bars inferred from the DPL fit (orange star) illustrate how the limited constraining power of our data at the faint end of the UVLF increases the uncertainty in  $\rho_{UV}$ . While these uncertainties are in part driven by fits that match the bright end of the UVLF, but are inconsistent with constraints from the literature at the faint end (see the orange shaded regions in Figure 7, top left panel), fixing the DPL slopes and turnover magnitude to the values found by Donnan et al. (2024) likely causes us to underestimate the true uncertainty in  $\rho_{UV}$ . Nevertheless, our measurement at  $z \sim 13$ , and the upper limit at  $z \sim 17$  indicate a somewhat more rapid evolution of the cSFRD at  $z \sim 10 - 17$  than found previously, while still being consistent with literature values within error bars at  $z \sim 13$ . Our  $2\sigma$  upper limit at  $z \sim 17$  is just below the  $1\sigma$  uncertainty from Pérez-González et al. (2025), indicating a more rapid drop of the cSFRD beyond  $z \sim 14$  than suggested by their measurement.

All models presented in Figure 8 are consistent with our measurement at  $z \sim 10$ , in particular if the generous error bars from the full DPL fit are considered. We note that we only show a subset of the models shown in Figure 7: the fiducial models, and those that best match our UVLFs from Somerville et al. (2025), Mauerhofer et al. (2025) and Hutter et al. (2025) respectively. At  $z \sim 13$ , most models are consistent with our measurement, with the baseline model from Somerville et al. (2025) lying below and the eSFE model from Mauerhofer et al. (2025) above. The latter, as well as the evolving IMF model from Hutter et al. (2025) lie above our upper limit at  $z \sim 17$ . Models that consistently reproduce our measured UV luminosity density across all redshifts are the AFM from Ferrara et al. (2023), the DMSFE model with  $f_d = 0.1$  from Somerville et al. (2025), the Salpeter IMF model from Hutter et al. (2025), and the fiducial model from Mauerhofer et al. (2025). In line with our discussion of the modeled UVLFs above, only small tweaks to the fiducial models, if at all, are required to match the abundance of galaxies we observe at  $z \gtrsim 10$ .

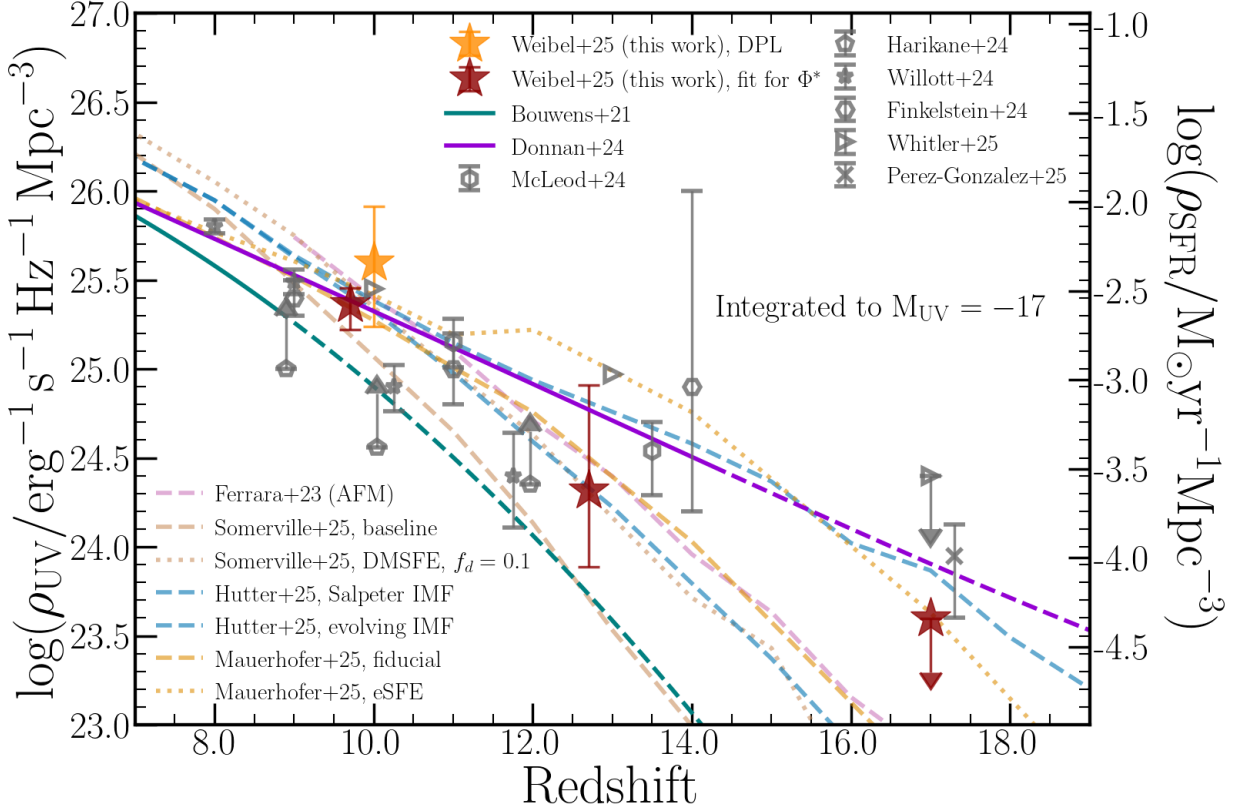


**Figure 8.** UV luminosity density obtained from integrating the fitted parametric curves, compared to various results from the literature (McLeod et al. 2024; Harikane et al. 2024; Willott et al. 2024; Finkelstein et al. 2024; Whittler et al. 2025; Pérez-González et al. 2025), and theoretical work, where we show a subset of the models displayed on the right of Figure 7: the AFM from Ferrara et al. (2023), the baseline and the DMSFE model with  $f_d = 0.1$  from Somerville et al. (2025), the Salpeter and the evolving IMF model from Hutter et al. (2025), as well as the fiducial and the eSFE model from Mauerhofer et al. (2025). The parametrizations from Bouwens et al. (2021) and Donnan et al. (2024) are shown as the blue and dark violet line respectively, where the extrapolated part is dashed. The secondary y-axis shows the cSFRD, based on the conversion factor from Madau & Dickinson (2014).

#### 4. DISCUSSION

In summary, we find UVLFs that are consistent with JWST-based literature results at  $z \sim 10$ , and confirm the high abundance of UV-bright ( $M_{UV} \sim -22$ ) galaxies with better number statistics and mitigated cosmic variance effects. We then find somewhat lower number densities at  $z \sim 13$ , especially at  $M_{UV} \sim -20$ , and provide the most constraining upper limits on the number density at  $z \sim 17$  to date. Together, these measurements suggest a more rapid evolution in the abundance of galaxies, and the UV luminosity density, than found previously. Comparing these findings to theoretical models shows that fiducial models that match the UVLF at  $z \sim 10$ , only need to be tweaked slightly to match our constraints at  $z \sim 13$  and beyond. We discuss some remaining caveats and limitations of this study below, before providing some additional interpretation of our results.

#### 4.1. Caveats and Limitations

##### 4.1.1. Inhomogeneous Filter Coverage

While our color-based sample selection described in Section 2.3 largely relies on the NIRCcam wide filters F115W, F150W, F200W, F277W, F356W, and F444W that are available across all fields used in this work, the inhomogeneous coverage by other filters nevertheless affects our results. First, the F410M filter is available across all legacy fields, as well as for the deepest five PANORAMIC pointings. Further, additional medium band filters are available for parts of the GOODS fields as well as the EGS, UDS, and COSMOS fields and the A2744 cluster (see Section 2.1 for a list of programs that contributed imaging to these fields). The additional filters help to break degeneracies in the *eazy* fits, and therefore enable a more robust removal of low- $z$  interlopers based on the  $z_{\text{phot}}$  probability distribution function.

Second, filters probing wavelengths below the Lyman break at  $z \gtrsim 9$  are available from JWST (F090W for



all the legacy fields, F070W for a small fraction), and HST (ACS and WFC3 across most of the legacy fields). They help rule out low- $z$  interlopers in two ways: again, by improving the photometric redshift constraints, and additionally during the visual inspection, by identifying sources with clearly visible flux in filters below the supposed Lyman break. The availability of additional filters therefore improves the quality of our selection over certain parts of the fields, in particular the legacy fields. At the same time, we would expect a higher interloper fraction in PANORAMIC pointings with imaging in only six wide filters.

As a test on the robustness of “6-filter-only” photometric redshifts at  $z \sim 10$ , we run **eazy** on the part of the Abell-2744 cluster field that is covered by the Mega Science program, meaning that all NIRCcam medium bands, as well as HST/ACS filters are available. We take the resulting photometric redshifts that have been shown to be robust out to at least  $z \sim 7$  in [Naidu et al. \(2024\)](#) through NIRCcam/grism spectroscopy as the ground truth, and then re-run **eazy** on just the PRIMER filter set (HST/ACS + 7 NIRCcam wide filters from F090W to F444W, and F410M), and on just the PANORAMIC filter set (6 NIRCcam wide filters from F115W - F444W). Applying our F115W dropout selection, we identify 9 high- $z$  candidates, 3 of which are confidently fit at low redshift with both the full and the PRIMER filter set. 2 out of those 3 with low- $z$  solutions are fit at  $z \gtrsim 9$  when using just the PANORAMIC filter set. This means that if we had selected F115W dropouts using the PANORAMIC filter set, we would have selected 8, 2 of which are low- $z$  interlopers, corresponding to a contamination fraction of 25%. For comparison, the HST pure parallel program BoRG ([Bradley et al. 2012](#)) specified contamination fractions ranging from  $\sim 40\%$  to  $\sim 90\%$  for dropout-selected  $z \sim 9 - 10$  galaxies at H-band magnitudes of 24.8 to 26.5, highlighting the substantial improvement that JWST provides in selecting  $z \sim 9 - 10$  galaxies from pure parallel imaging.

We note that possible remaining interlopers in our sample would boost the measured UVLF. Therefore, removing any interlopers would further strengthen our conclusion of relatively low number densities compared to other recent literature results, in particular at  $z \sim 13$ .

#### 4.1.2. $z \sim 13$ Candidates with Extended Morphology

During visual inspection, we identified 3 galaxies in our  $z \sim 13$  sample that are confidently fit at high redshift, and show an extended morphology and relatively low surface brightness. We show the photometry, SEDs and imaging cutouts of the three sources in Figure 9 in analogy to Figures 3 and 4.

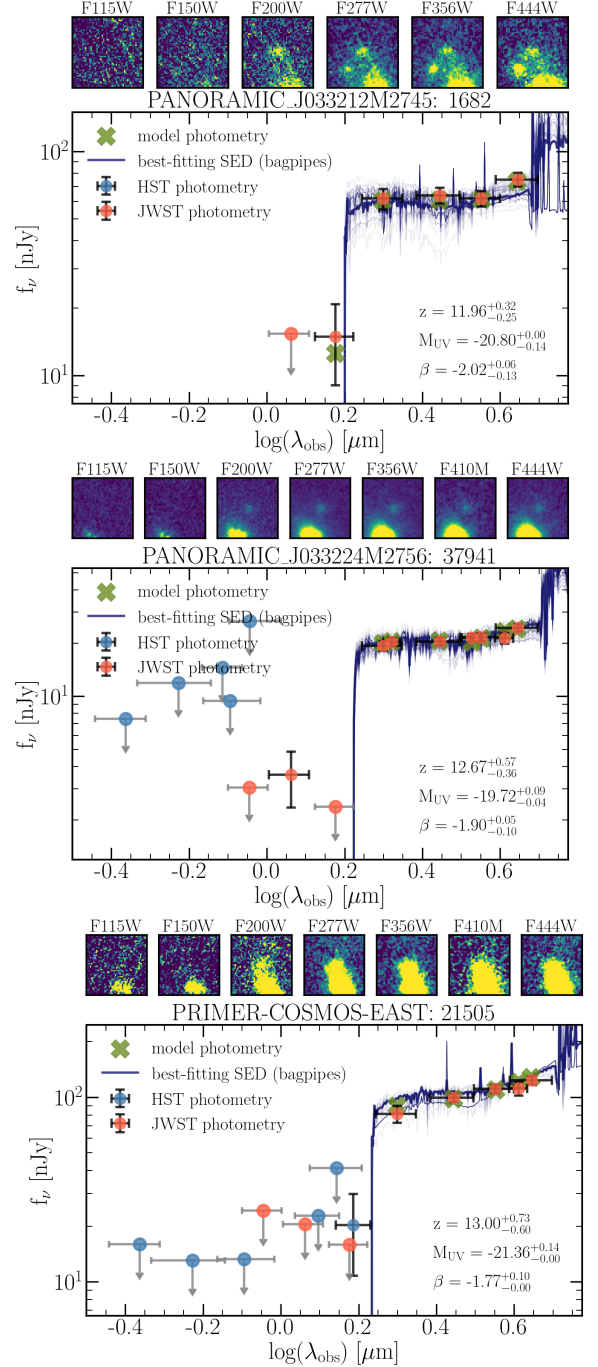


**Figure 9.** Three F150W dropout  $z \sim 13$  candidates from PANORAMIC and PRIMER-COSMOS, in analogy to Figures 3 and 4. They all show extended morphologies, and relatively low surface brightness, and they are located next to a bright galaxy whose  $z_{\text{phot}}$  is consistent with  $z \sim 3.4 - 3.5$ , a typical contaminant redshift of our F150W dropout sample.

All of them are located close to a brighter galaxy whose photometric redshift from **eazy** is consistent with  $z \sim 3.4 - 3.5$ . This redshift is common among low-redshift interlopers in our  $z \sim 13$  sample, due to  $H\beta$  and  $[O\text{ III}]$  boosting F200W, and  $H\alpha$  boosting F277W, and F356W, while F444W roughly probes the rest-frame optical to near-infrared continuum, mimicking a blue UV-continuum at  $z \sim 13$ .

We remove ID 21505 from our sample before computing the UVLF, as it is the brightest, and most extended of the three, while also being most strongly blended with the brighter neighboring galaxy. Further, it shows moderately red colors in the supposed UV-continuum, with  $F200W - F444W = 0.46$  which is close to the edge of our selection box at 0.5. This results in a UV-slope of  $\beta = 1.76 \pm 0.12$  which is atypical for galaxies at  $z \sim 13$  (e.g. Topping et al. 2024). Including this object would further boost the number density in the brightest bin at  $z \sim 13$ . We keep the other two sources in our sample and note here that removing them would yield a lower number density in the intermediate bin at  $z \sim 13$  ( $M_{UV} \sim -20$ ).

#### 4.1.3. Sparse Sampling of the Selection Function

In our completeness calculation, we assign completeness values to each source by sampling intrinsic properties ( $M_{UV}$ ,  $z$ , and  $\beta$ ) from the **bagpipes** posterior distribution, and then simulating the selection by creating mock photometry and adding noise to each filter according to the noise in our photometric catalog. The resulting completeness depends on the intrinsic properties, and the noise properties of the images in different filters. This statistically provides accurate correction factors for the effective volume from which we select galaxies. For example, when computing our UVLFs, we divide by the volume given by the survey area in a given bin of  $M_{UV}$  (Section 2.11), and the nominal redshift range of our sample (Section 2.3). In practice, the effectively sampled volume is smaller due to the incompleteness of our selection towards the edges of the nominal redshift range.

Accurately correcting for the incompleteness requires sufficient number statistics to sample the selection function along several dimensions ( $M_{UV}$ ,  $z$ ,  $\beta$ , and in principle, the noise level in different filters that are part of our selection). A single “outlier” at the edge of the nominal redshift range can be assigned a low completeness and significantly boost the UVLF. Conversely, the lack of such galaxies can lead to an overestimation of the effective survey volume and thus an underestimation of the UVLF. The same is true for the noise properties. Galaxies selected close to the selection threshold get as-

signed low values of completeness which are statistically correct, but can significantly affect the UVLF for small sample sizes. We mitigate effects of low completeness values by capping the inferred selection completeness at a somewhat arbitrary value of 0.02. Changing this value only significantly affects the inferred number density in the faintest  $M_{UV}$  bin respectively. Lowering it below 0.02 slightly boosts the number density in that bin, while also increasing the uncertainty. We argue that completeness values  $\lesssim 0.02$  cannot be reliably inferred given our setup, and that this problem can only be solved with larger samples of faint galaxies at high redshift, which are not the focus of this work. The number densities we measure at  $M_{UV} \lesssim -20$  are largely insensitive to the completeness correction.

#### 4.2. A Rapidly Evolving Galaxy Population at $z > 10$ ?

Compared to previous literature results, we find that the number density of galaxies at  $M_{UV} \lesssim -18.5$  drops relatively rapidly from  $z \sim 10$  to  $z \sim 13$  and beyond. This is also reflected in a more rapid decline of the UV luminosity density (Figure 8) where our results are however still consistent with most literature results within uncertainties. This is mostly because  $\rho_{UV}$  depends on the faint-end slope of the UVLF which is not well constrained by our data, and sensitive to the completeness correction discussed in the previous Section. For our fiducial measurements, we have adopted the UVLF parametrization from Donnan et al. (2024) which gives  $\alpha_{DPL} = -2.1$  at  $z = 12.7$ . We have tested that if we instead assume a steeper faint-end slope of  $\alpha_{DPL} = -2.6$ , as found e.g., at  $z \sim 10$  in Whitler et al. (2025), this only increases our inferred UV-luminosity density by  $\sim 0.1$  dex at  $z \sim 13$  which does not significantly change our finding of a more rapid decline compared to other results.

We note however, that in the brightest bin at  $z \sim 13$ , we measure a number density that is consistent with (e.g. Donnan et al. 2024) who measured it at  $z \sim 12.5$ . Moreover, 3 out of 4 galaxies in that bin lie at photometric redshifts  $> 14$ , with one of them spectroscopically confirmed at  $z = 14.1796$  (Carniani et al. 2024a,b). This indicates that the number density we would infer at the bright end of the UVLF would be similar at  $z \sim 14$ , suggesting a slow evolution in the number density of the very brightest galaxies ( $M_{UV} \lesssim -21$ ). This further results in a shallow bright-end slope of the UVLF which is also seen at  $z \sim 10$  where a Schechter function does not provide a good fit to the data due to the lack of an exponential cut-off out to  $M_{UV} \sim -22$ . Spectroscopic follow-up of the remaining two bright candidates at  $z \sim 14$ , and deep JWST imaging data over larger

areas, which may be obtained efficiently through pure parallel imaging in future cycles of JWST observations, are required to shed more light on the rapid build-up of these surprisingly luminous sources.

Our UVLFs are then qualitatively consistent with the picture outlined in [Donnan et al. \(2025\)](#), where the abundance of galaxies at the bright end of the UVLF is related to the ever younger ages of the stellar populations in galaxies at  $z \gtrsim 10$ . In terms of the modeling of the UVLF from [Shuntov et al. \(2025\)](#) (Section 3.4.1), it is the parameter  $\kappa_{UV}$ , used to convert between the SFR and UV luminosity, that is usually assumed to be fixed to the value from [Madau & Dickinson \(2014\)](#), which is based on a stellar population age of 100 Myr. As we approach the first galaxies, the average age of their stellar populations is however expected to drop below 100 Myr, which then boosts the UV luminosity at a given SFR.

The average ages assumed in [Donnan et al. \(2025\)](#) suggest a formation redshift of  $z \sim 15$ , meaning that they predict a rapid decline in the number density of galaxies at  $z > 15$ , following the rapid evolution of the halo mass function. This may be in line with the relatively rapid decline we find from  $z \sim 10$  to  $z \sim 13$  and certainly with the lack of candidates at  $z \sim 17$ . Whether this scenario can also account for the presence of the brightest galaxies at  $z \sim 14$  remains to be investigated.

## 5. SUMMARY AND CONCLUSIONS

Combining NIRCcam imaging data from legacy fields and the pure parallel program PANORAMIC, we perform measurements of the UVLF at  $z \gtrsim 9$  over the largest survey area to date ( $0.28 \text{ deg}^2$ ) with deep NIRCcam imaging in 6 or more filters, and along 35 independent lines of sight.

We start by selecting robust photometric candidates using a color-color selection that requires a strong Lyman break ( $> 1.5 \text{ mag}$  with a  $2\sigma$  upper limit in the dropout filter), and a  $\text{SNR} > 8$  red-wards of the break. After removing confident low redshift interlopers based on photometric redshifts from **eazy**, and visually vetting our samples, we identify 86 F115W dropouts ( $z \sim 10$ ), 11 F150W dropouts ( $z \sim 13$ ) and no robust F200W dropouts ( $z \sim 17$ ).

We perform SED-fitting with **bagpipes** to infer the UV properties for our entire galaxy sample. Sampling from the resulting posterior distributions, taking into account the incompleteness of our samples, as well as measuring the survey area as a function of the  $M_{UV}$  limit that can be probed across all survey fields, we infer UVLFs, as well as the UV-luminosity density at  $z \sim 10$ ,  $z \sim 13$ , and  $z \sim 17$ .

Our findings can be summarized as follows,

- Cross-matching with publicly available NIRSpectra, we find that 28 of our F115W and F150W dropout candidates have robust spectroscopic redshifts, and all of them are confirmed to be at  $z \gtrsim 9$ . Two of our F200W dropout candidates are spectroscopically confirmed to be low-redshift interlopers, one of them a previously unpublished source at  $z_{\text{spec}} = 4.9$  from CAPERS.
- We identify 14 new and robust candidates at  $z \sim 10$ , as well as two candidates at  $z \sim 14$  from PANORAMIC pure parallel imaging. If confirmed, the latter two sources may be the brightest sources known at this redshift, and break the current redshift record.
- Our UVLF at  $z \sim 10$  is consistent with a wealth of literature results, confirming a high abundance of UV-bright galaxies ( $M_{UV} \lesssim -21$ ) with better number statistics. At  $z \sim 13$ , we find somewhat lower number densities compared to most literature results, in particular at  $M_{UV} \sim -20$ . This suggests a rapid evolution in the number density from  $z \sim 10 - 13$ , reflected in a drop by an order of magnitude in the UV luminosity density over these redshifts.
- Our upper limits on the UV luminosity density at  $z \sim 17$  are the most constraining limits available to date, yielding  $\log(\rho_{UV}/\text{erg}^{-1}\text{s}^{-1}\text{Hz}^{-1}\text{Mpc}^{-3}) < 23.60$ , which implies that  $\rho_{UV}$  increases by at least a factor  $\sim 50$  from  $z \sim 17$  to  $z \sim 10$ .
- This indicates a rapid build-up of the galaxy population from  $z \gtrsim 15$  to the surprising presence of  $M_{UV} \sim -21$  galaxies at  $z \sim 14$ , and the high abundance of even more luminous galaxies at  $z \sim 10$ .
- Comparing these findings to models and simulations suggests that only a modest boost to fiducial modeled UVLFs in the recent literature is required to match the observed number densities of galaxies at  $z \gtrsim 10$ . This boost is achievable through enhanced burstiness of star formation, a more top-heavy IMF, a higher star formation efficiency, a lack of dust attenuation, or a combination thereof, perhaps limited to galaxies or regions within galaxies with high gas densities.

We have illustrated the power of combining deep legacy imaging data over large contiguous fields with pure parallel imaging that adds many independent lines of sight to constrain the properties of the galaxy population at  $z \gtrsim 9$ . The large available area allows us to

apply conservative color-based selection cuts, yielding robust samples of high redshift galaxies while maintaining reasonable number statistics. The independent lines of sight not only mitigate the effect of cosmic variance on the measured number density of galaxies, but also allow for a direct measurement of the clustering strength at  $z \sim 10$ , which can help discriminate between different models proposed to explain the abundance of UV-bright galaxies at  $z \gtrsim 10$ . We will explore this in an upcoming paper (Weibel & Jespersen et al. in prep.).

The measurements presented here are based on the largest currently available imaging area that enables the robust high- $z$  selections we performed. Further breakthroughs on the bright end of the UVLF at  $z \gtrsim 9$  will require larger samples, that must be collected from ever-larger deep NIRCcam imaging area. In the future, such expansion of area will be a critical resource for confirming our finding of a rapid decline in the abundance of galaxies at  $z > 10$ , and in placing stronger constraints at  $z \gtrsim 14$ , where only very few, but remarkably bright galaxies are known to date. At the same time, identified candidates must be followed up spectroscopically, to test and confirm photometry-based results and to better characterize the still poorly understood populations of low redshift interlopers contaminating dropout searches at  $z \gtrsim 11$ .

#### ACKNOWLEDGEMENTS

This work is based on observations made with the NASA/ESA/CSA James Webb Space Telescope. The

data were obtained from the Mikulski Archive for Space Telescopes at the Space Telescope Science Institute, which is operated by the Association of Universities for Research in Astronomy, Inc., under NASA contract NAS 5-03127 for JWST. These observations are associated with program #2514. The Cosmic Dawn Center is funded by the Danish National Research Foundation (DNRF140). This work has received funding from the Swiss State Secretariat for Education, Research and Innovation (SERI) under contract number MB22.00072, as well as from the Swiss National Science Foundation (SNSF) through project grant 200020\_207349. The work of CCW is supported by NOIRLab, which is managed by the Association of Universities for Research in Astronomy (AURA) under a cooperative agreement with the National Science Foundation. Support for program JWST-GO-2514 was provided by NASA through a grant from the Space Telescope Science Institute, which is operated by the Association of Universities for Research in Astronomy, Inc., under NASA contract NAS 5-03127.

*Facilities:* JWST(NIRSpec, NIRCcam)

*Software:* All software packages used in this work are publicly available on Github: `grizli`, `msafit`, `msaexp`. We acknowledge: `astropy` (Astropy Collaboration et al. 2013, 2018, 2022), `matplotlib` (Hunter 2007), `numpy` (Harris et al. 2020), `scipy` (Virtanen et al. 2020), `cosmic-variance` (Jespersen et al. 2025), the `jwst` pipeline (Bushouse et al. 2024), `msaexp` (Brammer 2024a), and `grizli` (Brammer 2024b)

#### REFERENCES

- Adams, N. J., Conselice, C. J., Ferreira, L., et al. 2023, MNRAS, 518, 4755, doi: [10.1093/mnras/stac3347](https://doi.org/10.1093/mnras/stac3347)
- Adams, N. J., Conselice, C. J., Austin, D., et al. 2024, ApJ, 965, 169, doi: [10.3847/1538-4357/ad2a7b](https://doi.org/10.3847/1538-4357/ad2a7b)
- Adams, N. J., Austin, D., Harvey, T., et al. 2025, arXiv e-prints, arXiv:2502.10282, doi: [10.48550/arXiv.2502.10282](https://doi.org/10.48550/arXiv.2502.10282)
- Akins, H. B., Casey, C. M., Lambrides, E., et al. 2024, arXiv e-prints, arXiv:2406.10341, doi: [10.48550/arXiv.2406.10341](https://doi.org/10.48550/arXiv.2406.10341)
- Anderson, J. 2016, Empirical Models for the WFC3/IR PSF, Instrument Science Report WFC3 2016-12, 42 pages
- Anderson, J., & King, I. R. 2000, PASP, 112, 1360, doi: [10.1086/316632](https://doi.org/10.1086/316632)
- Arrabal Haro, P., Dickinson, M., Finkelstein, S. L., et al. 2023, Nature, 622, 707, doi: [10.1038/s41586-023-06521-7](https://doi.org/10.1038/s41586-023-06521-7)
- Asada, Y., Willott, C., Muzzin, A., et al. 2025, Earliest Galaxy Evolution in the CANUCS+Technicolor fields: Galaxy Properties at  $z \sim 10 - 16$  seen with the Full NIRCcam Medium and Broad Band Filters. <https://arxiv.org/abs/2507.03124>
- Astropy Collaboration, Robitaille, T. P., Tollerud, E. J., et al. 2013, A&A, 558, A33, doi: [10.1051/0004-6361/201322068](https://doi.org/10.1051/0004-6361/201322068)
- Astropy Collaboration, Price-Whelan, A. M., Sipőcz, B. M., et al. 2018, AJ, 156, 123, doi: [10.3847/1538-3881/aabc4f](https://doi.org/10.3847/1538-3881/aabc4f)
- Astropy Collaboration, Price-Whelan, A. M., Lim, P. L., et al. 2022, ApJ, 935, 167, doi: [10.3847/1538-4357/ac7c74](https://doi.org/10.3847/1538-4357/ac7c74)
- Atek, H., Chemerynska, I., Wang, B., et al. 2023, MNRAS, 524, 5486, doi: [10.1093/mnras/stad1998](https://doi.org/10.1093/mnras/stad1998)
- Behroozi, P., Wechsler, R. H., Hearin, A. P., & Conroy, C. 2019, MNRAS, 488, 3143, doi: [10.1093/mnras/stz1182](https://doi.org/10.1093/mnras/stz1182)
- Bertin, E., & Arnouts, S. 1996, A&AS, 117, 393, doi: [10.1051/aas:1996164](https://doi.org/10.1051/aas:1996164)



- Bezanson, R., Labbe, I., Whitaker, K. E., et al. 2024, *ApJ*, 974, 92, doi: [10.3847/1538-4357/ad66cf](https://doi.org/10.3847/1538-4357/ad66cf)
- Bouwens, R. J., Illingworth, G. D., Labbe, I., et al. 2011, *Nature*, 469, 504, doi: [10.1038/nature09717](https://doi.org/10.1038/nature09717)
- Bouwens, R. J., Illingworth, G. D., Oesch, P. A., et al. 2014, *ApJ*, 793, 115, doi: [10.1088/0004-637X/793/2/115](https://doi.org/10.1088/0004-637X/793/2/115)
- Bouwens, R. J., Oesch, P. A., Labbé, I., et al. 2016, *ApJ*, 830, 67, doi: [10.3847/0004-637X/830/2/67](https://doi.org/10.3847/0004-637X/830/2/67)
- Bouwens, R. J., Oesch, P. A., Stefanon, M., et al. 2021, *AJ*, 162, 47, doi: [10.3847/1538-3881/abf83e](https://doi.org/10.3847/1538-3881/abf83e)
- Boylan-Kolchin, M. 2024, arXiv e-prints, arXiv:2407.10900, doi: [10.48550/arXiv.2407.10900](https://doi.org/10.48550/arXiv.2407.10900)
- Bradley, L., Sipőcz, B., Robitaille, T., et al. 2022, *astropy/photutils: 1.5.0*, 1.5.0, Zenodo, doi: [10.5281/zenodo.6825092](https://doi.org/10.5281/zenodo.6825092)
- Bradley, L. D., Trenti, M., Oesch, P. A., et al. 2012, *ApJ*, 760, 108, doi: [10.1088/0004-637X/760/2/108](https://doi.org/10.1088/0004-637X/760/2/108)
- Brammer, G. 2023a, *grizli*, 1.9.11, Zenodo, Zenodo, doi: [10.5281/zenodo.8370018](https://doi.org/10.5281/zenodo.8370018)
- . 2023b, *msaexp: NIRSpec analysis tools*, 0.6.17, Zenodo, doi: [10.5281/zenodo.7299500](https://doi.org/10.5281/zenodo.7299500)
- Brammer, G. 2024a, *msaexp: NIRSpec analysis tools*, 0.8.5, Zenodo, doi: [10.5281/zenodo.7299500](https://doi.org/10.5281/zenodo.7299500)
- . 2024b, *grizli*, 1.11.9, Zenodo, doi: [10.5281/zenodo.1146904](https://doi.org/10.5281/zenodo.1146904)
- Brammer, G. B., van Dokkum, P. G., & Coppi, P. 2008, *The Astrophysical Journal*, 686, 1503
- Brammer, G. B., van Dokkum, P. G., Illingworth, G. D., et al. 2013, *ApJL*, 765, L2, doi: [10.1088/2041-8205/765/1/L2](https://doi.org/10.1088/2041-8205/765/1/L2)
- Bunker, A. J., Saxena, A., Cameron, A. J., et al. 2023, *A&A*, 677, A88, doi: [10.1051/0004-6361/202346159](https://doi.org/10.1051/0004-6361/202346159)
- Bushouse, H., Eisenhamer, J., Dencheva, N., et al. 2024, *JWST Calibration Pipeline*, 1.14.0, Zenodo, doi: [10.5281/zenodo.10870758](https://doi.org/10.5281/zenodo.10870758)
- Calzetti, D., Armus, L., Bohlin, R. C., et al. 2000, *ApJ*, 533, 682, doi: [10.1086/308692](https://doi.org/10.1086/308692)
- Carnall, A. C., McLure, R. J., Dunlop, J. S., & Davé, R. 2018, *MNRAS*, 480, 4379, doi: [10.1093/mnras/sty2169](https://doi.org/10.1093/mnras/sty2169)
- Carnall, A. C., Begley, R., McLeod, D. J., et al. 2023a, *MNRAS*, 518, L45, doi: [10.1093/mnrasl/slac136](https://doi.org/10.1093/mnrasl/slac136)
- Carnall, A. C., McLure, R. J., Dunlop, J. S., et al. 2023b, *Nature*, 619, 716, doi: [10.1038/s41586-023-06158-6](https://doi.org/10.1038/s41586-023-06158-6)
- Carniani, S., Hainline, K., D'Eugenio, F., et al. 2024a, *Nature*, 633, 318, doi: [10.1038/s41586-024-07860-9](https://doi.org/10.1038/s41586-024-07860-9)
- Carniani, S., D'Eugenio, F., Ji, X., et al. 2024b, arXiv e-prints, arXiv:2409.20533, doi: [10.48550/arXiv.2409.20533](https://doi.org/10.48550/arXiv.2409.20533)
- Carrasco, D., Trenti, M., Mutch, S., & Oesch, P. A. 2018, *PASA*, 35, e022, doi: [10.1017/pasa.2018.17](https://doi.org/10.1017/pasa.2018.17)
- Casey, C. M., Kartaltepe, J. S., Drakos, N. E., et al. 2023, *ApJ*, 954, 31, doi: [10.3847/1538-4357/acc2bc](https://doi.org/10.3847/1538-4357/acc2bc)
- Casey, C. M., Akins, H. B., Shuntov, M., et al. 2024, *ApJ*, 965, 98, doi: [10.3847/1538-4357/ad2075](https://doi.org/10.3847/1538-4357/ad2075)
- Castellano, M., Fontana, A., Treu, T., et al. 2022, *ApJL*, 938, L15, doi: [10.3847/2041-8213/ac94d0](https://doi.org/10.3847/2041-8213/ac94d0)
- Castellano, M., Napolitano, L., Fontana, A., et al. 2024, *ApJ*, 972, 143, doi: [10.3847/1538-4357/ad5f88](https://doi.org/10.3847/1538-4357/ad5f88)
- Castellano, M., Fontana, A., Merlin, E., et al. 2025, arXiv e-prints, arXiv:2504.05893, <https://arxiv.org/abs/2504.05893>
- Chen, W., Kelly, P., Broadhurst, T., et al. 2022, *Transient Name Server AstroNote*, 260, 1
- Chuang, C.-Y., Jespersen, C. K., Lin, Y.-T., Ho, S., & Genel, S. 2024, *ApJ*, 965, 101, doi: [10.3847/1538-4357/ad2b6c](https://doi.org/10.3847/1538-4357/ad2b6c)
- Ciesla, L., Elbaz, D., Ilbert, O., et al. 2024, *A&A*, 686, A128, doi: [10.1051/0004-6361/202348091](https://doi.org/10.1051/0004-6361/202348091)
- Cole, J. W., Papovich, C., Finkelstein, S. L., et al. 2023, arXiv e-prints, arXiv:2312.10152, doi: [10.48550/arXiv.2312.10152](https://doi.org/10.48550/arXiv.2312.10152)
- Conroy, C., & Gunn, J. E. 2010, *ApJ*, 712, 833, doi: [10.1088/0004-637X/712/2/833](https://doi.org/10.1088/0004-637X/712/2/833)
- Conroy, C., Gunn, J. E., & White, M. 2009, *ApJ*, 699, 486, doi: [10.1088/0004-637X/699/1/486](https://doi.org/10.1088/0004-637X/699/1/486)
- Cueto, E. R., Hutter, A., Dayal, P., et al. 2024, *A&A*, 686, A138, doi: [10.1051/0004-6361/202349017](https://doi.org/10.1051/0004-6361/202349017)
- Curtis-Lake, E., Carniani, S., Cameron, A., et al. 2023, *Nature Astronomy*, 7, 622, doi: [10.1038/s41550-023-01918-w](https://doi.org/10.1038/s41550-023-01918-w)
- Dayal, P., Ferrara, A., Dunlop, J. S., & Pacucci, F. 2014, *MNRAS*, 445, 2545, doi: [10.1093/mnras/stu1848](https://doi.org/10.1093/mnras/stu1848)
- DeCoursey, C., Egami, E., Pierel, J. D. R., et al. 2025, *ApJ*, 979, 250, doi: [10.3847/1538-4357/ad8fab](https://doi.org/10.3847/1538-4357/ad8fab)
- Dekel, A., Sarkar, K. C., Birnboim, Y., Mandelker, N., & Li, Z. 2023, *MNRAS*, 523, 3201, doi: [10.1093/mnras/stad1557](https://doi.org/10.1093/mnras/stad1557)
- Donnan, C. T., Dunlop, J. S., McLure, R. J., McLeod, D. J., & Cullen, F. 2025, arXiv e-prints, arXiv:2501.03217, doi: [10.48550/arXiv.2501.03217](https://doi.org/10.48550/arXiv.2501.03217)
- Donnan, C. T., McLeod, D. J., Dunlop, J. S., et al. 2023, *MNRAS*, 518, 6011, doi: [10.1093/mnras/stac3472](https://doi.org/10.1093/mnras/stac3472)
- Donnan, C. T., McLure, R. J., Dunlop, J. S., et al. 2024, *MNRAS*, 533, 3222, doi: [10.1093/mnras/stae2037](https://doi.org/10.1093/mnras/stae2037)
- Eisenstein, D. J., Willott, C., Alberts, S., et al. 2023a, arXiv e-prints, arXiv:2306.02465, doi: [10.48550/arXiv.2306.02465](https://doi.org/10.48550/arXiv.2306.02465)
- Eisenstein, D. J., Johnson, B. D., Robertson, B., et al. 2023b, arXiv e-prints, arXiv:2310.12340, doi: [10.48550/arXiv.2310.12340](https://doi.org/10.48550/arXiv.2310.12340)

- Eldridge, J. J., Stanway, E. R., Xiao, L., et al. 2017, *PASA*, 34, e058, doi: [10.1017/pasa.2017.51](https://doi.org/10.1017/pasa.2017.51)
- Ellis, R. S., McLure, R. J., Dunlop, J. S., et al. 2013, *ApJL*, 763, L7, doi: [10.1088/2041-8205/763/1/L7](https://doi.org/10.1088/2041-8205/763/1/L7)
- Ferland, G. J., Chatzikos, M., Guzmán, F., et al. 2017, *RMxAA*, 53, 385, doi: [10.48550/arXiv.1705.10877](https://doi.org/10.48550/arXiv.1705.10877)
- Ferrara, A., Pallottini, A., & Dayal, P. 2023, *MNRAS*, 522, 3986, doi: [10.1093/mnras/stad1095](https://doi.org/10.1093/mnras/stad1095)
- Finkelstein, S. L., Bagley, M. B., Ferguson, H. C., et al. 2023, *ApJL*, 946, L13, doi: [10.3847/2041-8213/acade4](https://doi.org/10.3847/2041-8213/acade4)
- Finkelstein, S. L., Leung, G. C. K., Bagley, M. B., et al. 2024, *ApJL*, 969, L2, doi: [10.3847/2041-8213/ad4495](https://doi.org/10.3847/2041-8213/ad4495)
- Finkelstein, S. L., Bagley, M. B., Arrabal Haro, P., et al. 2025, arXiv e-prints, arXiv:2501.04085, doi: [10.48550/arXiv.2501.04085](https://doi.org/10.48550/arXiv.2501.04085)
- Fujimoto, S., Wang, B., Weaver, J. R., et al. 2024, *ApJ*, 977, 250, doi: [10.3847/1538-4357/ad9027](https://doi.org/10.3847/1538-4357/ad9027)
- Furtak, L. J., Zitrin, A., Weaver, J. R., et al. 2023, *MNRAS*, 523, 4568, doi: [10.1093/mnras/stad1627](https://doi.org/10.1093/mnras/stad1627)
- Gardner, J. P., Mather, J. C., Abbott, R., et al. 2023, *PASP*, 135, 068001, doi: [10.1088/1538-3873/acd1b5](https://doi.org/10.1088/1538-3873/acd1b5)
- Gehrels, N. 1986, *ApJ*, 303, 336, doi: [10.1086/164079](https://doi.org/10.1086/164079)
- Greene, J. E., Labbe, I., Goulding, A. D., et al. 2024, *ApJ*, 964, 39, doi: [10.3847/1538-4357/ad1e5f](https://doi.org/10.3847/1538-4357/ad1e5f)
- Hainline, K. N., Johnson, B. D., Robertson, B., et al. 2024, *ApJ*, 964, 71, doi: [10.3847/1538-4357/ad1ee4](https://doi.org/10.3847/1538-4357/ad1ee4)
- Harikane, Y., Nakajima, K., Ouchi, M., et al. 2024, *ApJ*, 960, 56, doi: [10.3847/1538-4357/ad0b7e](https://doi.org/10.3847/1538-4357/ad0b7e)
- Harikane, Y., Inoue, A. K., Mawatari, K., et al. 2022, *ApJ*, 929, 1, doi: [10.3847/1538-4357/ac53a9](https://doi.org/10.3847/1538-4357/ac53a9)
- Harikane, Y., Ouchi, M., Oguri, M., et al. 2023, *ApJS*, 265, 5, doi: [10.3847/1538-4365/acaaa9](https://doi.org/10.3847/1538-4365/acaaa9)
- Harikane, Y., Inoue, A. K., Ellis, R. S., et al. 2025, *ApJ*, 980, 138, doi: [10.3847/1538-4357/ad9b2c](https://doi.org/10.3847/1538-4357/ad9b2c)
- Harris, C. R., Millman, K. J., van der Walt, S. J., et al. 2020, *Nature*, 585, 357, doi: [10.1038/s41586-020-2649-2](https://doi.org/10.1038/s41586-020-2649-2)
- Hegde, S., Wyatt, M. M., & Furlanetto, S. R. 2024, *JCAP*, 2024, 025, doi: [10.1088/1475-7516/2024/08/025](https://doi.org/10.1088/1475-7516/2024/08/025)
- Heintz, K. E., Brammer, G. B., Watson, D., et al. 2025, *A&A*, 693, A60, doi: [10.1051/0004-6361/202450243](https://doi.org/10.1051/0004-6361/202450243)
- Hinshaw, G., Larson, D., Komatsu, E., et al. 2013, *ApJS*, 208, 19, doi: [10.1088/0067-0049/208/2/19](https://doi.org/10.1088/0067-0049/208/2/19)
- Hunter, J. D. 2007, *Computing in Science and Engineering*, 9, 90, doi: [10.1109/MCSE.2007.55](https://doi.org/10.1109/MCSE.2007.55)
- Hutter, A., Cueto, E. R., Dayal, P., et al. 2025, *A&A*, 694, A254, doi: [10.1051/0004-6361/202452460](https://doi.org/10.1051/0004-6361/202452460)
- Inoue, A. K., Shimizu, I., Iwata, I., & Tanaka, M. 2014, *MNRAS*, 442, 1805, doi: [10.1093/mnras/stu936](https://doi.org/10.1093/mnras/stu936)
- Ishigaki, M., Kawamata, R., Ouchi, M., et al. 2018, *ApJ*, 854, 73, doi: [10.3847/1538-4357/aaa544](https://doi.org/10.3847/1538-4357/aaa544)
- Jespersen, C. K., Cranmer, M., Melchior, P., et al. 2022, *ApJ*, 941, 7, doi: [10.3847/1538-4357/ac9b18](https://doi.org/10.3847/1538-4357/ac9b18)
- Jespersen, C. K., Steinhardt, C. L., Somerville, R. S., & Lovell, C. C. 2025, *ApJ*, 982, 23, doi: [10.3847/1538-4357/adb422](https://doi.org/10.3847/1538-4357/adb422)
- Jeřábková, T., Zonoozi, A. H., Kroupa, P., et al. 2018, *A&A*, 620, A39, doi: [10.1051/0004-6361/201833055](https://doi.org/10.1051/0004-6361/201833055)
- Ji, X., Maiolino, R., Übler, H., et al. 2025, arXiv e-prints, arXiv:2501.13082, doi: [10.48550/arXiv.2501.13082](https://doi.org/10.48550/arXiv.2501.13082)
- Katz, H., Ji, A. P., Telford, G., & Senchyna, P. 2024, *The Open Journal of Astrophysics*, 7, 106, doi: [10.33232/001c.126253](https://doi.org/10.33232/001c.126253)
- Kocevski, D. D., Finkelstein, S. L., Barro, G., et al. 2024, arXiv e-prints, arXiv:2404.03576, doi: [10.48550/arXiv.2404.03576](https://doi.org/10.48550/arXiv.2404.03576)
- Kokorev, V., Atek, H., Chisholm, J., et al. 2024a, arXiv e-prints, arXiv:2411.13640, doi: [10.48550/arXiv.2411.13640](https://doi.org/10.48550/arXiv.2411.13640)
- Kokorev, V., Caputi, K. I., Greene, J. E., et al. 2024b, *ApJ*, 968, 38, doi: [10.3847/1538-4357/ad4265](https://doi.org/10.3847/1538-4357/ad4265)
- Kravtsov, A., & Belokurov, V. 2024, arXiv e-prints, arXiv:2405.04578, doi: [10.48550/arXiv.2405.04578](https://doi.org/10.48550/arXiv.2405.04578)
- Kroupa, P., Tout, C. A., & Gilmore, G. 1993, *MNRAS*, 262, 545, doi: [10.1093/mnras/262.3.545](https://doi.org/10.1093/mnras/262.3.545)
- Labbe, I., Greene, J. E., Bezanson, R., et al. 2025, *ApJ*, 978, 92, doi: [10.3847/1538-4357/ad3551](https://doi.org/10.3847/1538-4357/ad3551)
- Leethochawalit, N., Trenti, M., Morishita, T., Roberts-Borsani, G., & Treu, T. 2022, *MNRAS*, 509, 5836, doi: [10.1093/mnras/stab3265](https://doi.org/10.1093/mnras/stab3265)
- Leja, J., Carnall, A. C., Johnson, B. D., Conroy, C., & Speagle, J. S. 2019, *ApJ*, 876, 3, doi: [10.3847/1538-4357/ab133c](https://doi.org/10.3847/1538-4357/ab133c)
- Leung, G. C. K., Bagley, M. B., Finkelstein, S. L., et al. 2023, *ApJL*, 954, L46, doi: [10.3847/2041-8213/acf365](https://doi.org/10.3847/2041-8213/acf365)
- Li, Z., Dekel, A., Sarkar, K. C., et al. 2024, *A&A*, 690, A108, doi: [10.1051/0004-6361/202348727](https://doi.org/10.1051/0004-6361/202348727)
- Looser, T. J., D'Eugenio, F., Maiolino, R., et al. 2023, arXiv e-prints, arXiv:2306.02470, doi: [10.48550/arXiv.2306.02470](https://doi.org/10.48550/arXiv.2306.02470)
- . 2024, *Nature*, 629, 53, doi: [10.1038/s41586-024-07227-0](https://doi.org/10.1038/s41586-024-07227-0)
- Lu, S., Frenk, C. S., Bose, S., et al. 2025, *MNRAS*, 536, 1018, doi: [10.1093/mnras/stae2646](https://doi.org/10.1093/mnras/stae2646)
- Madau, P., & Dickinson, M. 2014, *ARA&A*, 52, 415, doi: [10.1146/annurev-astro-081811-125615](https://doi.org/10.1146/annurev-astro-081811-125615)
- Madau, P., Ferguson, H. C., Dickinson, M. E., et al. 1996, *MNRAS*, 283, 1388, doi: [10.1093/mnras/283.4.1388](https://doi.org/10.1093/mnras/283.4.1388)
- Mason, C. A., Trenti, M., & Treu, T. 2015, *ApJ*, 813, 21, doi: [10.1088/0004-637X/813/1/21](https://doi.org/10.1088/0004-637X/813/1/21)
- . 2023, *MNRAS*, 521, 497, doi: [10.1093/mnras/stad035](https://doi.org/10.1093/mnras/stad035)

- Matthee, J., Naidu, R. P., Brammer, G., et al. 2024, *ApJ*, 963, 129, doi: [10.3847/1538-4357/ad2345](https://doi.org/10.3847/1538-4357/ad2345)
- Mauerhofer, V., Dayal, P., Haehnelt, M. G., et al. 2025, *A&A*, 696, A157, doi: [10.1051/0004-6361/202554042](https://doi.org/10.1051/0004-6361/202554042)
- Maxwell, E. A. 2011, arXiv e-prints, arXiv:1102.0822, doi: [10.48550/arXiv.1102.0822](https://doi.org/10.48550/arXiv.1102.0822)
- McLeod, D. J., McLure, R. J., & Dunlop, J. S. 2016, *MNRAS*, 459, 3812, doi: [10.1093/mnras/stw904](https://doi.org/10.1093/mnras/stw904)
- McLeod, D. J., Donnan, C. T., McLure, R. J., et al. 2024, *MNRAS*, 527, 5004, doi: [10.1093/mnras/stad3471](https://doi.org/10.1093/mnras/stad3471)
- Meurer, G. R., Heckman, T. M., & Calzetti, D. 1999, *ApJ*, 521, 64, doi: [10.1086/307523](https://doi.org/10.1086/307523)
- Morishita, T., Mason, C. A., Kreilgaard, K. C., et al. 2025, *ApJ*, 983, 152, doi: [10.3847/1538-4357/adbbdc](https://doi.org/10.3847/1538-4357/adbbdc)
- Moster, B. P., Somerville, R. S., Newman, J. A., & Rix, H.-W. 2011, *ApJ*, 731, 113, doi: [10.1088/0004-637X/731/2/113](https://doi.org/10.1088/0004-637X/731/2/113)
- Naidu, R. P., Oesch, P. A., van Dokkum, P., et al. 2022a, *ApJL*, 940, L14, doi: [10.3847/2041-8213/ac9b22](https://doi.org/10.3847/2041-8213/ac9b22)
- Naidu, R. P., Oesch, P. A., Setton, D. J., et al. 2022b, arXiv e-prints, arXiv:2208.02794, doi: [10.48550/arXiv.2208.02794](https://doi.org/10.48550/arXiv.2208.02794)
- Naidu, R. P., Matthee, J., Kramarenko, I., et al. 2024, arXiv e-prints, arXiv:2410.01874, doi: [10.48550/arXiv.2410.01874](https://doi.org/10.48550/arXiv.2410.01874)
- Naidu, R. P., Oesch, P. A., Brammer, G., et al. 2025, arXiv e-prints, arXiv:2505.11263, <https://arxiv.org/abs/2505.11263>
- Napolitano, L., Castellano, M., Pentericci, L., et al. 2025, *A&A*, 693, A50, doi: [10.1051/0004-6361/202452090](https://doi.org/10.1051/0004-6361/202452090)
- Narayanan, D., Stark, D. P., Finkelstein, S. L., et al. 2025, *ApJ*, 982, 7, doi: [10.3847/1538-4357/adb41c](https://doi.org/10.3847/1538-4357/adb41c)
- Oesch, P. A., Bouwens, R. J., Illingworth, G. D., Labbé, I., & Stefanon, M. 2018, *ApJ*, 855, 105, doi: [10.3847/1538-4357/aab03f](https://doi.org/10.3847/1538-4357/aab03f)
- Oesch, P. A., Bouwens, R. J., Illingworth, G. D., et al. 2014, *ApJ*, 786, 108, doi: [10.1088/0004-637X/786/2/108](https://doi.org/10.1088/0004-637X/786/2/108)
- Oesch, P. A., Brammer, G., van Dokkum, P. G., et al. 2016, *ApJ*, 819, 129, doi: [10.3847/0004-637X/819/2/129](https://doi.org/10.3847/0004-637X/819/2/129)
- Oesch, P. A., Brammer, G., Naidu, R. P., et al. 2023, *MNRAS*, 525, 2864, doi: [10.1093/mnras/stad2411](https://doi.org/10.1093/mnras/stad2411)
- Pacucci, F., Dayal, P., Harikane, Y., Inoue, A. K., & Loeb, A. 2022, *MNRAS*, 514, L6, doi: [10.1093/mnrasl/slac035](https://doi.org/10.1093/mnrasl/slac035)
- Pérez-González, P. G., Costantin, L., Langeroodi, D., et al. 2023, *ApJL*, 951, L1, doi: [10.3847/2041-8213/acd9d0](https://doi.org/10.3847/2041-8213/acd9d0)
- Pérez-González, P. G., Östlin, G., Costantin, L., et al. 2025, arXiv e-prints, arXiv:2503.15594, doi: [10.48550/arXiv.2503.15594](https://doi.org/10.48550/arXiv.2503.15594)
- Perrin, M. D., Sivaramakrishnan, A., Lajoie, C.-P., et al. 2014, in *Society of Photo-Optical Instrumentation Engineers (SPIE) Conference Series*, Vol. 9143, *Space Telescopes and Instrumentation 2014: Optical, Infrared, and Millimeter Wave*, ed. J. Oschmann, Jacobus M., M. Clampin, G. G. Fazio, & H. A. MacEwen, 91433X, doi: [10.1117/12.2056689](https://doi.org/10.1117/12.2056689)
- Price, S. H., Bezanson, R., Labbe, I., et al. 2025, *ApJ*, 982, 51, doi: [10.3847/1538-4357/adaec1](https://doi.org/10.3847/1538-4357/adaec1)
- Rieke, M. J., Kelly, D. M., Misselt, K., et al. 2023, *PASP*, 135, 028001, doi: [10.1088/1538-3873/acac53](https://doi.org/10.1088/1538-3873/acac53)
- Roberts-Borsani, G., Bagley, M., Rojas-Ruiz, S., et al. 2024a, arXiv e-prints, arXiv:2407.17551, doi: [10.48550/arXiv.2407.17551](https://doi.org/10.48550/arXiv.2407.17551)
- Roberts-Borsani, G., Treu, T., Shapley, A., et al. 2024b, arXiv e-prints, arXiv:2403.07103, doi: [10.48550/arXiv.2403.07103](https://doi.org/10.48550/arXiv.2403.07103)
- Robertson, B., Johnson, B. D., Tacchella, S., et al. 2024, *ApJ*, 970, 31, doi: [10.3847/1538-4357/ad463d](https://doi.org/10.3847/1538-4357/ad463d)
- Rojas-Ruiz, S., Bagley, M. B., Roberts-Borsani, G., et al. 2024, arXiv e-prints, arXiv:2408.00843, doi: [10.48550/arXiv.2408.00843](https://doi.org/10.48550/arXiv.2408.00843)
- Rosdahl, J., Blaizot, J., Katz, H., et al. 2022, *MNRAS*, 515, 2386, doi: [10.1093/mnras/stac1942](https://doi.org/10.1093/mnras/stac1942)
- Salim, S., Boquien, M., & Lee, J. C. 2018, *ApJ*, 859, 11, doi: [10.3847/1538-4357/aabf3c](https://doi.org/10.3847/1538-4357/aabf3c)
- Schechter, P. 1976, *ApJ*, 203, 297, doi: [10.1086/154079](https://doi.org/10.1086/154079)
- Schouws, S., Bouwens, R. J., Ormerod, K., et al. 2024, arXiv e-prints, arXiv:2409.20549, doi: [10.48550/arXiv.2409.20549](https://doi.org/10.48550/arXiv.2409.20549)
- Serjeant, S., & Bakx, T. J. L. C. 2023, *Nature Astronomy*, 7, 1143, doi: [10.1038/s41550-023-02093-8](https://doi.org/10.1038/s41550-023-02093-8)
- Shen, X., Vogelsberger, M., Boylan-Kolchin, M., Tacchella, S., & Kannan, R. 2023, *MNRAS*, 525, 3254, doi: [10.1093/mnras/stad2508](https://doi.org/10.1093/mnras/stad2508)
- Shuntov, M., Oesch, P. A., Toft, S., et al. 2025, arXiv e-prints, arXiv:2503.14280, doi: [10.48550/arXiv.2503.14280](https://doi.org/10.48550/arXiv.2503.14280)
- Somerville, R. S., & Primack, J. R. 1999, *MNRAS*, 310, 1087, doi: [10.1046/j.1365-8711.1999.03032.x](https://doi.org/10.1046/j.1365-8711.1999.03032.x)
- Somerville, R. S., Primack, J. R., & Faber, S. M. 2001, *MNRAS*, 320, 504, doi: [10.1046/j.1365-8711.2001.03975.x](https://doi.org/10.1046/j.1365-8711.2001.03975.x)
- Somerville, R. S., Yung, L. Y. A., Lancaster, L., et al. 2025, arXiv e-prints, arXiv:2505.05442, doi: [10.48550/arXiv.2505.05442](https://doi.org/10.48550/arXiv.2505.05442)
- Song, M., Finkelstein, S. L., Ashby, M. L. N., et al. 2016, *ApJ*, 825, 5, doi: [10.3847/0004-637X/825/1/5](https://doi.org/10.3847/0004-637X/825/1/5)
- Stanway, E. R., & Eldridge, J. J. 2018, *MNRAS*, 479, 75, doi: [10.1093/mnras/sty1353](https://doi.org/10.1093/mnras/sty1353)

- Steidel, C. C., Giallisco, M., Pettini, M., Dickinson, M., & Adelberger, K. L. 1996, *ApJL*, 462, L17, doi: [10.1086/310029](https://doi.org/10.1086/310029)
- Strait, V., Brammer, G., Muzzin, A., et al. 2023, *ApJL*, 949, L23, doi: [10.3847/2041-8213/acd457](https://doi.org/10.3847/2041-8213/acd457)
- Suess, K. A., Weaver, J. R., Price, S. H., et al. 2024, *ApJ*, 976, 101, doi: [10.3847/1538-4357/ad75fe](https://doi.org/10.3847/1538-4357/ad75fe)
- Sun, G., Faucher-Giguère, C.-A., Hayward, C. C., et al. 2023, *ApJL*, 955, L35, doi: [10.3847/2041-8213/acf85a](https://doi.org/10.3847/2041-8213/acf85a)
- Tacchella, S., Bose, S., Conroy, C., Eisenstein, D. J., & Johnson, B. D. 2018, *ApJ*, 868, 92, doi: [10.3847/1538-4357/aae8e0](https://doi.org/10.3847/1538-4357/aae8e0)
- Tacchella, S., Conroy, C., Faber, S. M., et al. 2022, *ApJ*, 926, 134, doi: [10.3847/1538-4357/ac449b](https://doi.org/10.3847/1538-4357/ac449b)
- Taylor, A. J., Kokorev, V., Kocevski, D. D., et al. 2025, arXiv e-prints, arXiv:2505.04609, doi: [10.48550/arXiv.2505.04609](https://doi.org/10.48550/arXiv.2505.04609)
- Topping, M. W., Stark, D. P., Endsley, R., et al. 2024, *MNRAS*, 529, 4087, doi: [10.1093/mnras/stae800](https://doi.org/10.1093/mnras/stae800)
- Toyouchi, D., Yajima, H., Ferrara, A., & Nagamine, K. 2025, arXiv e-prints, arXiv:2502.12538, doi: [10.48550/arXiv.2502.12538](https://doi.org/10.48550/arXiv.2502.12538)
- Trapp, A. C., Furlanetto, S. R., & Yang, J. 2022, *MNRAS*, 510, 4844, doi: [10.1093/mnras/stab3801](https://doi.org/10.1093/mnras/stab3801)
- Treu, T., Roberts-Borsani, G., Bradac, M., et al. 2022, *ApJ*, 935, 110, doi: [10.3847/1538-4357/ac8158](https://doi.org/10.3847/1538-4357/ac8158)
- Trinca, A., Schneider, R., Valiante, R., et al. 2024, *MNRAS*, 529, 3563, doi: [10.1093/mnras/stae651](https://doi.org/10.1093/mnras/stae651)
- Valentino, F., Brammer, G., Gould, K. M. L., et al. 2023, *ApJ*, 947, 20, doi: [10.3847/1538-4357/acbefa](https://doi.org/10.3847/1538-4357/acbefa)
- Virtanen, P., Gommers, R., Oliphant, T. E., et al. 2020, *Nature Methods*, 17, 261, doi: [10.1038/s41592-019-0686-2](https://doi.org/10.1038/s41592-019-0686-2)
- Wang, B., Leja, J., de Graaff, A., et al. 2024, *ApJL*, 969, L13, doi: [10.3847/2041-8213/ad55f7](https://doi.org/10.3847/2041-8213/ad55f7)
- Watson, W. A., Iliev, I. T., D’Aloisio, A., et al. 2013, *MNRAS*, 433, 1230, doi: [10.1093/mnras/stt791](https://doi.org/10.1093/mnras/stt791)
- Weibel, A., Oesch, P. A., Barrufet, L., et al. 2024, *MNRAS*, 533, 1808, doi: [10.1093/mnras/stae1891](https://doi.org/10.1093/mnras/stae1891)
- Whitler, L., Stark, D. P., Topping, M. W., et al. 2025, arXiv e-prints, arXiv:2501.00984, doi: [10.48550/arXiv.2501.00984](https://doi.org/10.48550/arXiv.2501.00984)
- Williams, C. C., Curtis-Lake, E., Hainline, K. N., et al. 2018, *ApJS*, 236, 33, doi: [10.3847/1538-4365/aabcbb](https://doi.org/10.3847/1538-4365/aabcbb)
- Williams, C. C., Tacchella, S., Maseda, M. V., et al. 2023, *ApJS*, 268, 64, doi: [10.3847/1538-4365/acf130](https://doi.org/10.3847/1538-4365/acf130)
- Williams, C. C., Oesch, P. A., Weibel, A., et al. 2025, *ApJ*, 979, 140, doi: [10.3847/1538-4357/ad97bc](https://doi.org/10.3847/1538-4357/ad97bc)
- Willott, C. J., Doyon, R., Albert, L., et al. 2022, *PASP*, 134, 025002, doi: [10.1088/1538-3873/ac5158](https://doi.org/10.1088/1538-3873/ac5158)
- Willott, C. J., Desprez, G., Asada, Y., et al. 2024, *ApJ*, 966, 74, doi: [10.3847/1538-4357/ad35bc](https://doi.org/10.3847/1538-4357/ad35bc)
- Windhorst, R. A., Cohen, S. H., Jansen, R. A., et al. 2023, *AJ*, 165, 13, doi: [10.3847/1538-3881/aca163](https://doi.org/10.3847/1538-3881/aca163)
- Wu, J. F., Jespersen, C. K., & Wechsler, R. H. 2024, *ApJ*, 976, 37, doi: [10.3847/1538-4357/ad7bb3](https://doi.org/10.3847/1538-4357/ad7bb3)
- Yung, L. Y. A., Somerville, R. S., Finkelstein, S. L., Wilkins, S. M., & Gardner, J. P. 2024, *MNRAS*, 527, 5929, doi: [10.1093/mnras/stad3484](https://doi.org/10.1093/mnras/stad3484)
- Zavala, J. A., Buat, V., Casey, C. M., et al. 2023, *ApJL*, 943, L9, doi: [10.3847/2041-8213/acacfe](https://doi.org/10.3847/2041-8213/acacfe)
- Zitrin, A., Zheng, W., Broadhurst, T., et al. 2014, *ApJL*, 793, L12, doi: [10.1088/2041-8205/793/1/L12](https://doi.org/10.1088/2041-8205/793/1/L12)
- Zitrin, A., Fabris, A., Merten, J., et al. 2015, *ApJ*, 801, 44, doi: [10.1088/0004-637X/801/1/44](https://doi.org/10.1088/0004-637X/801/1/44)



## APPENDIX

## A. TABLES OF HIGH REDSHIFT CANDIDATES

We list our F115W dropout ( $z \sim 10$ ) and F150W dropout ( $z \sim 13$ ) candidates in tables 2 and 3. For each candidate we specify the ID, field, position, UV-magnitude (corrected for lensing magnification in the A2744 field), UV-slope, photometric redshifts from **eazy** and **bagpipes**, and the spectroscopic redshift from the DJA where available.

**Table 2.**  $z \sim 10$  F115W dropout candidates with ID, field, R.A, Declination,  $M_{UV}$ , UV-slope  $\beta$ ,  $z_{\text{phot, bp}}$  where the redshift is allowed to vary freely in the range (0,20),  $z_{\text{phot, bp}}$  from **bagpipes** where the redshift is constrained to the nominal range of the dropout selection, and  $z_{\text{spec}}$  from the DJA where available. The UV-magnitudes in the A2744 cluster field are corrected for lensing magnification (see Section 2.7).

ID	Field	R.A.	Decl.	$M_{UV}$	UV-slope $\beta$	$z_{\text{phot, bp}}$ (constr.)	$z_{\text{phot, eazy}}$ (free)	$z_{\text{spec}}$
4811	A2744	3.5930298	-30.4497638	$-19.27^{+0.07}_{-0.06}$	$-2.65^{+0.05}_{-0.06}$	$10.60^{+0.23}_{-0.26}$	$10.57^{+0.17}_{-0.36}$	-
4995	A2744	3.6375685	-30.4491546	$-20.78^{+0.12}_{-0.07}$	$-2.65^{+0.10}_{-0.08}$	$10.17^{+0.31}_{-0.42}$	$9.33^{+0.89}_{-0.06}$	-
10719	A2744	3.5653689	-30.4323244	$-19.25^{+0.00}_{-0.00}$	$-2.65^{+0.00}_{-0.00}$	$9.15^{+0.20}_{-0.00}$	$9.38^{+0.52}_{-0.09}$	-
13534	A2744	3.6171746	-30.425549	$-21.81^{+0.04}_{-0.01}$	$-2.42^{+0.09}_{-0.04}$	$9.37^{+0.03}_{-0.02}$	$9.46^{+0.03}_{-0.04}$	$9.32 \pm 0.67$
25365	A2744	3.5901109	-30.3597408	$-19.96^{+0.04}_{-0.03}$	$-2.69^{+0.05}_{-0.04}$	$10.46^{+0.12}_{-0.11}$	$10.48^{+0.10}_{-0.18}$	$10.39 \pm 0.01$
33044	A2744	3.5119258	-30.3718616	$-20.48^{+0.03}_{-0.03}$	$-2.12^{+0.05}_{-0.08}$	$10.40^{+0.08}_{-0.25}$	$9.92^{+0.34}_{-0.10}$	-
33292	A2744	3.6295118	-30.3721366	$-19.15^{+0.09}_{-0.10}$	$-2.49^{+0.10}_{-0.09}$	$9.27^{+0.44}_{-0.15}$	$9.23^{+0.93}_{-0.06}$	-
37210	A2744	3.5670696	-30.3778665	$-18.59^{+0.06}_{-0.05}$	$-2.32^{+0.10}_{-0.07}$	$10.19^{+0.20}_{-0.07}$	$10.11^{+0.30}_{-0.30}$	$10.06 \pm 0.01$
49489	A2744	3.5925024	-30.4014645	$-18.12^{+0.04}_{-0.05}$	$-2.52^{+0.07}_{-0.07}$	$9.83^{+0.11}_{-0.09}$	$9.88^{+0.11}_{-0.10}$	$9.80 \pm 0.01$
55963	A2744	3.4513634	-30.320718	$-19.96^{+0.01}_{-0.07}$	$-2.64^{+0.00}_{-0.04}$	$10.50^{+0.00}_{-0.20}$	$10.09^{+0.32}_{-0.25}$	$10.40 \pm 0.42$
56436	A2744	3.4514157	-30.321808	$-20.68^{+0.05}_{-0.04}$	$-2.64^{+0.04}_{-0.05}$	$10.57^{+0.11}_{-0.16}$	$10.44^{+0.14}_{-0.49}$	$10.23 \pm 0.01$
67453	A2744	3.4787409	-30.3455347	$-19.84^{+0.04}_{-0.09}$	$-2.50^{+0.13}_{-0.10}$	$10.51^{+0.19}_{-0.16}$	$10.43^{+0.14}_{-0.89}$	$10.11 \pm 0.01$
11360	COSMOS	150.1165619	2.1970808	$-20.89^{+0.01}_{-0.10}$	$-2.55^{+0.08}_{-0.07}$	$9.82^{+0.16}_{-0.08}$	$9.88^{+0.14}_{-0.22}$	-
44352	COSMOS	150.1625774	2.3091963	$-20.53^{+0.12}_{-0.06}$	$-2.46^{+0.08}_{-0.10}$	$9.50^{+0.35}_{-0.31}$	$9.59^{+0.42}_{-0.24}$	-
50134	COSMOS	150.0723028	2.2378703	$-19.66^{+0.05}_{-0.05}$	$-2.35^{+0.08}_{-0.05}$	$9.62^{+0.38}_{-0.11}$	$9.62^{+0.59}_{-0.07}$	-
67414	COSMOS	150.0731262	2.2560541	$-20.09^{+0.04}_{-0.03}$	$-2.25^{+0.07}_{-0.09}$	$10.28^{+0.24}_{-0.42}$	$10.65^{+0.11}_{-0.57}$	-
82389	COSMOS	150.1263736	2.3837847	$-20.96^{+0.04}_{-0.03}$	$-2.47^{+0.06}_{-0.05}$	$8.91^{+0.03}_{-0.05}$	$8.88^{+0.05}_{-0.04}$	-
91271	COSMOS	150.1623425	2.3573897	$-20.64^{+0.09}_{-0.08}$	$-2.19^{+0.10}_{-0.16}$	$9.50^{+0.99}_{-0.29}$	$2.71^{+0.04}_{-0.40}$	-
18031	EGS	214.8118509	52.7371107	$-20.41^{+0.09}_{-0.11}$	$-2.22^{+0.10}_{-0.10}$	$9.98^{+0.34}_{-0.50}$	$9.70^{+0.28}_{-0.18}$	$9.57 \pm 0.28$
38537	EGS	214.7728188	52.7408645	$-20.53^{+0.07}_{-0.09}$	$-2.43^{+0.13}_{-0.11}$	$9.23^{+0.16}_{-0.19}$	$9.31^{+0.19}_{-0.08}$	-
62111	EGS	214.994398	52.9893815	$-20.16^{+0.08}_{-0.05}$	$-2.57^{+0.09}_{-0.13}$	$9.24^{+0.11}_{-0.14}$	$9.21^{+0.15}_{-0.11}$	-
78312	EGS	214.9773607	52.9264978	$-20.59^{+0.12}_{-0.08}$	$-2.35^{+0.08}_{-0.07}$	$9.37^{+0.48}_{-0.20}$	$9.22^{+0.15}_{-0.23}$	$9.03 \pm 0.52$
85166	EGS	214.732526	52.7580908	$-20.38^{+0.05}_{-0.10}$	$-2.57^{+0.10}_{-0.08}$	$10.22^{+0.16}_{-0.45}$	$10.06^{+0.29}_{-0.30}$	$9.85 \pm 0.00$
20969	GOODS-N	189.3373968	62.180731	$-19.90^{+0.05}_{-0.03}$	$-2.47^{+0.06}_{-0.06}$	$9.23^{+0.06}_{-0.09}$	$9.26^{+0.89}_{-0.04}$	-
31580	GOODS-N	189.2176887	62.1994938	$-20.12^{+0.03}_{-0.08}$	$-2.56^{+0.05}_{-0.01}$	$9.92^{+0.22}_{-0.20}$	$9.79^{+0.16}_{-0.18}$	$9.75 \pm 0.01$
32549	GOODS-N	189.2620124	62.2010893	$-19.87^{+0.05}_{-0.05}$	$-2.51^{+0.01}_{-0.07}$	$9.54^{+0.23}_{-0.07}$	$9.56^{+0.17}_{-0.15}$	-
38008	GOODS-N	189.2397961	62.210828	$-19.96^{+0.05}_{-0.03}$	$-2.69^{+0.05}_{-0.02}$	$10.26^{+0.01}_{-0.24}$	$10.12^{+0.15}_{-0.16}$	$9.63 \pm 0.01$
38123	GOODS-N	189.2391136	62.2109319	$-19.99^{+0.05}_{-0.05}$	$-2.56^{+0.06}_{-0.06}$	$10.09^{+0.27}_{-0.15}$	$10.09^{+0.17}_{-0.13}$	$9.75 \pm 0.01$
38138	GOODS-N	189.2392329	62.2109669	$-19.73^{+0.09}_{-0.08}$	$-2.56^{+0.06}_{-0.06}$	$9.69^{+0.20}_{-0.24}$	$9.58^{+0.26}_{-0.17}$	-
44181	GOODS-N	189.1582478	62.22136	$-20.28^{+0.10}_{-0.07}$	$-2.47^{+0.07}_{-0.10}$	$9.54^{+0.30}_{-0.23}$	$9.41^{+0.17}_{-0.11}$	$9.08 \pm 0.54$
49123	GOODS-N	189.2890305	62.2290441	$-19.61^{+0.06}_{-0.11}$	$-1.89^{+0.22}_{-0.18}$	$9.94^{+0.02}_{-0.24}$	$9.62^{+0.20}_{-0.13}$	-

49306	GOODS-N	189.2887936	62.2292987	$-20.30^{+0.05}_{-0.07}$	$-2.49^{+0.05}_{-0.08}$	$10.02^{+0.31}_{-0.25}$	$9.78^{+0.22}_{-0.17}$	-
56195	GOODS-N	189.3447528	62.2395493	$-20.96^{+0.04}_{-0.04}$	$-2.28^{+0.08}_{-0.10}$	$9.53^{+0.19}_{-0.15}$	$9.53^{+0.16}_{-0.09}$	-
58504	GOODS-N	189.2177196	62.3117795	$-20.44^{+0.03}_{-0.04}$	$-2.26^{+0.04}_{-0.03}$	$9.49^{+0.19}_{-0.14}$	$9.40^{+0.22}_{-0.10}$	-
68946	GOODS-N	189.1383278	62.2898615	$-20.41^{+0.06}_{-0.06}$	$-2.62^{+0.04}_{-0.06}$	$9.32^{+0.07}_{-0.13}$	$9.32^{+0.11}_{-0.10}$	$9.31 \pm 0.66$
71038	GOODS-N	189.336496	62.2872732	$-20.69^{+0.05}_{-0.04}$	$-2.57^{+0.08}_{-0.05}$	$10.72^{+0.17}_{-0.05}$	$10.77^{+0.11}_{-0.23}$	-
99271	GOODS-N	189.1060584	62.2420546	$-22.11^{+0.03}_{-0.04}$	$-2.49^{+0.03}_{-0.03}$	$10.83^{+0.01}_{-0.11}$	$10.66^{+0.13}_{-0.13}$	$10.62 \pm 0.01$
20537	GOODS-S	53.1369587	-27.9223218	$-19.10^{+0.11}_{-0.06}$	$-2.67^{+0.08}_{-0.06}$	$8.92^{+0.15}_{-0.17}$	$2.29^{+6.75}_{-0.13}$	-
20594	GOODS-S	53.1755128	-27.7806394	$-19.91^{+0.00}_{-0.08}$	$-2.23^{+0.02}_{-0.22}$	$9.62^{+0.07}_{-0.01}$	$9.62^{+0.06}_{-0.12}$	$9.70 \pm 0.53$
20793	GOODS-S	53.2101891	-27.7811464	$-19.23^{+0.09}_{-0.10}$	$-2.58^{+0.12}_{-0.09}$	$9.88^{+0.37}_{-0.60}$	$9.98^{+0.16}_{-0.71}$	-
21022	GOODS-S	53.1429678	-27.9211781	$-19.43^{+0.14}_{-0.07}$	$-2.39^{+0.10}_{-0.08}$	$9.74^{+0.22}_{-0.30}$	$9.58^{+0.29}_{-0.11}$	-
21250	GOODS-S	53.0268097	-27.8944239	$-19.80^{+0.00}_{-0.07}$	$-2.67^{+0.16}_{-0.00}$	$10.71^{+0.00}_{-0.50}$	$9.22^{+1.08}_{-0.02}$	-
23803	GOODS-S	53.0558158	-27.8771828	$-19.80^{+0.05}_{-0.04}$	$-2.39^{+0.08}_{-0.08}$	$10.68^{+0.25}_{-0.15}$	$10.72^{+0.14}_{-0.24}$	-
30383	GOODS-S	53.0599901	-27.8851371	$-18.51^{+0.00}_{-0.00}$	$-2.64^{+0.01}_{-0.00}$	$9.92^{+0.05}_{-0.00}$	$9.51^{+0.53}_{-0.07}$	-
32068	GOODS-S	53.0517661	-27.8872656	$-19.14^{+0.00}_{-0.13}$	$-2.62^{+0.01}_{-0.07}$	$10.59^{+0.00}_{-0.56}$	$9.92^{+0.18}_{-0.30}$	-
37256	GOODS-S	53.0488536	-27.8943462	$-18.10^{+0.11}_{-0.08}$	$-2.56^{+0.08}_{-0.09}$	$9.41^{+0.52}_{-0.28}$	$9.31^{+0.67}_{-0.12}$	-
40653	GOODS-S	53.1222194	-27.899075	$-19.86^{+0.00}_{-0.11}$	$-2.04^{+0.00}_{-0.27}$	$10.21^{+0.04}_{-0.00}$	$8.95^{+1.56}_{-0.08}$	-
40797	GOODS-S	53.1520418	-27.894689	$-19.68^{+0.05}_{-0.00}$	$-2.34^{+0.06}_{-0.00}$	$10.35^{+0.07}_{-0.00}$	$10.16^{+0.23}_{-0.72}$	-
50841	GOODS-S	53.0747668	-27.8454149	$-17.95^{+0.15}_{-0.10}$	$-2.66^{+0.10}_{-0.06}$	$9.30^{+0.40}_{-0.21}$	$2.26^{+7.65}_{-0.06}$	-
52109	GOODS-S	53.1139227	-27.7958502	$-19.62^{+0.04}_{-0.03}$	$-2.66^{+0.04}_{-0.04}$	$9.29^{+0.07}_{-0.17}$	$9.32^{+0.11}_{-0.08}$	-
52254	GOODS-S	53.1105925	-27.8476813	$-18.99^{+0.16}_{-0.03}$	$-2.64^{+0.12}_{-0.07}$	$9.94^{+0.13}_{-0.55}$	$9.41^{+0.49}_{-0.13}$	-
53952	GOODS-S	53.1199264	-27.8463998	$-19.64^{+0.08}_{-0.00}$	$-2.01^{+0.17}_{-0.00}$	$10.05^{+0.00}_{-0.07}$	$8.70^{+1.57}_{-0.14}$	-
54919	GOODS-S	53.1336198	-27.8449854	$-20.90^{+0.03}_{-0.00}$	$-1.99^{+0.03}_{-0.00}$	$10.25^{+0.00}_{-0.02}$	$9.03^{+1.23}_{-0.04}$	$9.06 \pm 0.54$
56288	GOODS-S	53.0738751	-27.7967777	$-20.11^{+0.07}_{-0.08}$	$-2.29^{+0.06}_{-0.10}$	$9.48^{+0.49}_{-0.22}$	$9.33^{+0.34}_{-0.21}$	-
58181	GOODS-S	53.1673584	-27.8075081	$-19.45^{+0.05}_{-0.04}$	$-2.42^{+0.04}_{-0.10}$	$10.00^{+0.26}_{-0.26}$	$10.15^{+0.21}_{-0.32}$	-
58229	GOODS-S	53.0601956	-27.8562517	$-18.59^{+0.19}_{-0.03}$	$-2.69^{+0.09}_{-0.05}$	$9.79^{+0.81}_{-0.00}$	$10.03^{+0.30}_{-0.31}$	-
58640	GOODS-S	53.0760756	-27.856015	$-18.29^{+0.06}_{-0.09}$	$-2.61^{+0.14}_{-0.04}$	$9.49^{+0.56}_{-0.29}$	$9.38^{+0.74}_{-0.03}$	-
58713	GOODS-S	53.097475	-27.8569785	$-18.71^{+0.00}_{-0.00}$	$-2.77^{+0.00}_{-0.00}$	$9.70^{+0.00}_{-0.00}$	$9.91^{+0.12}_{-0.38}$	-
58944	GOODS-S	53.0974877	-27.8567695	$-18.48^{+0.19}_{-0.18}$	$-2.21^{+0.12}_{-0.31}$	$9.97^{+0.00}_{-0.26}$	$9.35^{+0.29}_{-0.23}$	-
62915	GOODS-S	53.1760302	-27.8173944	$-18.68^{+0.04}_{-0.09}$	$-1.89^{+0.11}_{-0.08}$	$10.00^{+0.08}_{-0.20}$	$8.72^{+1.59}_{-0.10}$	$8.69 \pm 0.15$
64456	GOODS-S	53.0677405	-27.8645459	$-18.58^{+0.11}_{-0.05}$	$-2.51^{+0.05}_{-0.06}$	$9.38^{+0.44}_{-0.19}$	$9.21^{+0.35}_{-0.16}$	-
70396	GOODS-S	53.06683	-27.8729315	$-20.20^{+0.07}_{-0.06}$	$-2.47^{+0.08}_{-0.08}$	$10.78^{+0.17}_{-0.20}$	$10.59^{+0.17}_{-0.23}$	-
72355	GOODS-S	53.1659346	-27.8342373	$-19.87^{+0.04}_{-0.05}$	$-2.52^{+0.13}_{-0.08}$	$10.86^{+0.26}_{-0.38}$	$10.85^{+0.21}_{-0.24}$	$10.42 \pm 0.12$
74275	GOODS-S	53.0677252	-27.8378687	$-19.87^{+0.08}_{-0.11}$	$-2.59^{+0.05}_{-0.05}$	$9.52^{+0.29}_{-0.25}$	$9.34^{+0.29}_{-0.13}$	$9.07 \pm 0.00$
77980	GOODS-S	53.0747796	-27.8448877	$-18.34^{+0.08}_{-0.17}$	$-2.57^{+0.07}_{-0.09}$	$9.95^{+0.55}_{-0.69}$	$10.26^{+0.34}_{-0.37}$	-
137	PANO-M0214	34.3559257	-2.1877144	$-20.81^{+0.03}_{-0.04}$	$-2.48^{+0.04}_{-0.12}$	$10.86^{+0.11}_{-0.24}$	$10.84^{+0.15}_{-1.64}$	-
2694	PANO-M0531	341.5438683	-5.4867792	$-19.91^{+0.07}_{-0.08}$	$-2.43^{+0.06}_{-0.08}$	$9.28^{+0.07}_{-0.22}$	$9.26^{+0.22}_{-6.89}$	-

5353	PANO-M1019	24.7385435	-10.3135874	$-20.46^{+0.06}_{-0.08}$	$-2.54^{+0.06}_{-0.07}$	$9.23^{+0.16}_{-0.24}$	$9.17^{+0.19}_{-6.84}$	-
8761	PANO-M2152	24.4682148	-21.8756005	$-20.78^{+0.08}_{-0.03}$	$-1.99^{+0.12}_{-0.40}$	$10.07^{+0.41}_{-0.69}$	$9.40^{+0.20}_{-0.08}$	-
9329	PANO-M2152	24.4640518	-21.878989	$-20.09^{+0.06}_{-0.09}$	$-2.29^{+0.04}_{-0.09}$	$9.79^{+0.31}_{-0.49}$	$9.36^{+0.49}_{-0.12}$	-
6429	PANO-M2409	64.0490774	-24.1677286	$-19.78^{+0.11}_{-0.06}$	$-2.53^{+0.10}_{-0.10}$	$9.44^{+0.14}_{-0.34}$	$9.26^{+0.43}_{-0.15}$	-
3805	PANO-P0025	334.2379492	0.4494868	$-20.40^{+0.04}_{-0.06}$	$-2.23^{+0.09}_{-0.10}$	$10.96^{+0.15}_{-0.16}$	$2.71^{+0.27}_{-0.20}$	-
14395	PANO-P0025	334.1687353	0.3967385	$-19.95^{+0.06}_{-0.06}$	$-2.32^{+0.12}_{-0.14}$	$9.60^{+0.10}_{-0.15}$	$9.61^{+0.40}_{-0.09}$	-
14904	PANO-P0025	334.2300049	0.4305707	$-20.00^{+0.13}_{-0.03}$	$-2.49^{+0.05}_{-0.03}$	$9.11^{+0.20}_{-0.10}$	$9.19^{+0.11}_{-0.12}$	-
30966	PANO-P0025	334.2430242	0.3876525	$-20.03^{+0.11}_{-0.05}$	$-2.50^{+0.06}_{-0.03}$	$9.64^{+0.37}_{-0.10}$	$9.98^{+0.12}_{-0.40}$	-
31622	PANO-P0025	334.2516193	0.3866468	$-19.16^{+0.14}_{-0.08}$	$-2.52^{+0.09}_{-0.11}$	$9.07^{+0.25}_{-0.31}$	$9.08^{+0.21}_{-0.32}$	-
2872	PANO-P0819	142.9597428	8.3305148	$-21.51^{+0.00}_{-0.07}$	$-2.26^{+0.00}_{-0.16}$	$9.16^{+0.03}_{-0.00}$	$9.29^{+0.18}_{-7.02}$	-
717	PANO-P5652	194.2691344	56.8795975	$-21.26^{+0.09}_{-0.00}$	$-2.62^{+0.05}_{-0.00}$	$8.97^{+0.37}_{-0.00}$	$9.32^{+0.60}_{-0.12}$	-
4710	UDS	34.4953911	-5.315862	$-21.40^{+0.01}_{-0.12}$	$-1.94^{+0.05}_{-0.07}$	$10.04^{+0.02}_{-0.63}$	$9.32^{+0.93}_{-0.12}$	-
11544	UDS	34.3248881	-5.3443945	$-21.40^{+0.13}_{-0.13}$	$-2.51^{+0.11}_{-0.08}$	$9.68^{+0.53}_{-0.75}$	$9.10^{+0.43}_{-0.17}$	-
18893	UDS	34.5209502	-5.2926626	$-20.47^{+0.06}_{-0.08}$	$-2.04^{+0.05}_{-0.10}$	$10.06^{+0.22}_{-0.24}$	$10.08^{+0.19}_{-0.44}$	-
21510	UDS	34.4266175	-5.2889423	$-20.71^{+0.07}_{-0.10}$	$-2.45^{+0.07}_{-0.11}$	$9.09^{+0.23}_{-0.14}$	$2.26^{+0.41}_{-0.29}$	-
33482	UDS	34.4349624	-5.2711199	$-20.70^{+0.00}_{-0.06}$	$-2.36^{+0.02}_{-0.07}$	$9.43^{+0.04}_{-0.06}$	$9.44^{+0.16}_{-0.08}$	$9.31 \pm 0.66$
52799	UDS	34.4135848	-5.2442305	$-20.27^{+0.09}_{-0.06}$	$-2.51^{+0.00}_{-0.13}$	$10.61^{+0.25}_{-0.01}$	$9.58^{+0.59}_{-0.25}$	$10.32 \pm 0.34$
89565	UDS	34.4602808	-5.1849891	$-20.67^{+0.04}_{-0.14}$	$-2.42^{+0.00}_{-0.09}$	$9.75^{+0.13}_{-0.58}$	$9.29^{+0.25}_{-0.09}$	$9.27 \pm 0.64$
118503	UDS	34.3058347	-5.1543431	$-20.32^{+0.05}_{-0.02}$	$-2.50^{+0.06}_{-0.07}$	$9.07^{+0.15}_{-0.11}$	$9.21^{+0.11}_{-0.09}$	$9.25 \pm 0.63$

**Table 3.** Same as Table 2, but for the  $z \sim 13$  F150W dropout candidates.

ID	Field	R.A.	Decl.	$M_{UV}$	UV-slope $\beta$	$Z_{\text{phot, bp}}$ (constr.)	$Z_{\text{phot, eazy}}$ (free)	$Z_{\text{spec}}$
57585	A2744	3.4989832	-30.3247598	$-20.82^{+0.07}_{-0.04}$	$-2.56^{+0.10}_{-0.08}$	$12.49^{+0.15}_{-0.08}$	$12.50^{+0.11}_{-0.11}$	$12.34 \pm 0.01$
13670	COSMOS	150.0611622	2.1607632	$-19.98^{+0.10}_{-0.18}$	$-2.41^{+0.22}_{-0.06}$	$13.06^{+0.69}_{-0.68}$	$12.53^{+1.09}_{-0.18}$	-
58174	COSMOS	150.0991743	2.2479515	$-20.06^{+0.02}_{-0.10}$	$-2.07^{+0.13}_{-0.06}$	$12.64^{+0.41}_{-0.45}$	$3.39^{+8.78}_{-0.15}$	-
89475	EGS	214.9136249	52.8800796	$-20.32^{+0.01}_{-0.07}$	$-2.53^{+0.04}_{-0.05}$	$13.61^{+0.24}_{-0.40}$	$12.38^{+1.22}_{-0.12}$	-
1682	GOODS-S	53.0108107	-27.7420301	$-20.80^{+0.00}_{-0.14}$	$-2.02^{+0.06}_{-0.13}$	$12.23^{+0.00}_{-0.36}$	$11.88^{+0.35}_{-0.55}$	-
37941	GOODS-S	53.0401901	-27.8964376	$-19.72^{+0.09}_{-0.04}$	$-1.90^{+0.05}_{-0.10}$	$12.77^{+0.56}_{-0.36}$	$12.50^{+1.04}_{-0.25}$	-
66144	GOODS-S	53.1663441	-27.8215581	$-18.90^{+0.15}_{-0.11}$	$-2.49^{+0.10}_{-0.06}$	$12.01^{+0.41}_{-0.36}$	$11.96^{+0.35}_{-0.25}$	$12.51 \pm 0.01$
69545	GOODS-S	53.0468267	-27.8718992	$-18.80^{+0.03}_{-0.19}$	$-2.14^{+0.15}_{-0.20}$	$12.62^{+0.96}_{-0.77}$	$11.85^{+1.59}_{-0.18}$	-
84448	GOODS-S	53.0829443	-27.8556285	$-21.28^{+0.01}_{-0.02}$	$-2.19^{+0.07}_{-0.08}$	$14.16^{+0.08}_{-0.08}$	$14.31^{+0.09}_{-0.11}$	$14.1796 \pm 0.0007$
35840	PANO-P0025	334.2503616	0.3792025	$-21.15^{+0.00}_{-0.00}$	$-2.44^{+0.00}_{-0.00}$	$14.51^{+0.00}_{-0.00}$	$14.47^{+0.18}_{-0.63}$	-
3640	PANO-P5549	205.9473187	55.802757	$-21.65^{+0.11}_{-0.23}$	$-2.52^{+0.16}_{-0.00}$	$13.57^{+0.71}_{-1.38}$	$12.10^{+1.89}_{-0.42}$	-